CHEMICAL REVIEWS

Review

pubs.acs.org/CR

ZnO Meso-Mechano-Thermo Physical Chemistry

Jianwei Li,[†] Shouzhi Ma,[‡] Xinjuan Liu,[§] Zhaofeng Zhou,[†] and Chang Q Sun*[,†,‡]

[†]Institute for Quantum Engineering and Micro-Nano Energy Technology, Key Laboratory of Low-Dimensional Materials and Application Technologies, and Faculty of Materials and Optoelectronics and Physics, Xiangtan University, Hunan 411105, China

[‡]School of Electrical, and Electronic Engineering, Nanyang Technological University, Singapore 639798

[§]Engineering Research Center for Nanophotonics & Advanced Instrument, Ministry of Education, Department of Physics, East China Normal University, Shanghai, 200062 China

CONTENTS

1. INTRODUCTION

1.1. Size and Defect Fascinations

ZnO is a kind of amazing material with multiple functions that have been investigated since the 1940s. With and without dopant substitution,[1] nanostructured ZnO exhibits strong piezoelectric[2] and dilute magnetic properties[3] dominating at sites of defects or varying with surface crystal morphology.[4] As a result, ZnO provides an impact on applications in upcoming technologies[5] such as biomedical sensors,[6] actuators,[7] solar cells,[8] catalysis,[9] energy harvesting,[10] photonic crystals,[11] supercapacitors,[12] lasers,[13] photodetectors,[14] drug carriers,[15] superhydrophobicity,[16] and light-emitting[17] devices due to its fascinating performance in electronics, optics, photonics, and magnetics.[18] Therefore, ZnO is regarded as one of the few materials dominating the upcoming technological thrusts.[19]

ZnO nanostructures have attracted much attention in recent years as they behave differently from their bulk counterpart. There are two categories of interest in the properties in addition to controllable growth of various shapes and surface textures.[20] One is the size dependency: the known properties of the bulk ZnO, such as the elastic modulus, band gap, etc., no longer remain constant but change with the size and shape of the solid specimen. The other is the defect-mediated emerging properties that the bulk does not demonstrate, such as dilute magnetism, enhanced catalytic ability, superhydrophobicity, etc. The fraction increase of the undercoordinated atoms and the stronger interaction between them as well as the valence charge distribution, densification, localization, and polarization should form the key to the interest.[4a,21]

The undercoordinated surface and defect atoms become dominant in determining the physical properties of nanostructures,[22] which result in variation in many properties, such as Young's modulus,[23] band gap,[24] critical temperature for phase transition and growth nucleation,[25] frequency shift of lattice vibration,[26] piezoelectricity,[10a,27] dielectric constant,[28] etc. The variation of the properties with respect to those of the bulk counterpart depends on the structural size and shape as well as the surface conditions. For example, Chen et al.[23a] discovered that the Young's modulus of ZnO nanowire of 17 nm across is 220 GPa compared with the bulk value of 144 GPa. Xu et al.[29]

Received: November 11, 2011
Published: February 16, 2012

   dx.doi.org/10.1021/cr200428m | *Chem. Rev.* 2012, 112, 2833−2852

found that both the tensile and the bending modulus of ZnO nanowires increase as the wire diameter is decreased from 80 to 20 nm. The bending modulus increases more rapidly than the tensile modulus due to surface stiffening. Agrawal et al.[23e] found that the elastic modulus of [0001]-oriented ZnO nanowires increases from 140 to 160 GPa as the nanowire diameter is decreased from 80 to 20 nm. Zang et al.[30] found that electron beam radiation can raise the elastic modulus of the ZnSnO wire by more than 40%. The tension experiments also showed that the fracture strain and strength of ZnO wire follow the same trend of size. Lin et al.[24a] found that the photoluminescence energy (E_{PL}) of ZnO nanocrystals increases from 3.30 to 3.43 eV and the photoabsorption energy (E_{PA}) increases from 3.43 to 3.65 eV as the size decreases from 12 to 3.5 nm. Similar trends of size-dependent optical properties have also been reported for ZnO nanodots,[23a,24c,31] nanorods,[24b,32] and nanobelts.[33] Yuan et al.[34] found two possible mechanisms for the surface texture-induced surface tension and charge-transferring dynamics that dictate the catalytic performance of ZnO nanostructures. On the other hand, these physical properties also change under external stimuli such as pressure and temperature.[32b,35]

1.2. State of the Art Knowledge

1.2.1. Size Dependency. Young's modulus (Y) is related to a material's properties such as elasticity, extensibility, acoustic transmission velocity, Debye temperature, specific heat, and thermal conductivity of the specimen. The mechanical strength is related intrinsically to the electronegativity[36] and ionicity[37] of the specimen; the electronegativity and iconicity determine the strength of the bonds between the constituting elements of the material. The change of Young's modulus with solid size is generally attributed to the variation of the surface to volume ratio;[38] the impact of surface atoms, with smaller effective interatomic radius due to the loss of surface bonds, is enormously profound.[38b]

Numerous sophisticated models have been developed to explain the size-induced elasticity of nanostructures. Liang et al.[39] suggested that the nonlinear response of the nanowire's core to the mechanical stimuli and the surface stress dominate the size dependency of Young's modulus. Agrawal et al.[23e] suggested that surface reconstruction together with long-range ionic interactions dominate the size-dependent elasticity of ZnO. Molecular dynamics (MD) simulations[39] of the square cross-sectional copper nanowires with side lengths ranging from 1.2 to 14.0 nm suggested the effects of surfaces and edges whose elastic properties deviated significantly from that of the corresponding bulk dictate the size dependency.[40] A core−shell composite model[23a] is frequently applied in describing the size-dependent Young's modulus with the shell or skin of about 2.4−4.4 nm thick.[23a,29]

Among the models for the photoluminescence (PL) blue shift of nanosemiconductors,[41] the elegantly accepted theory for the energy blue shift of a nanosemiconductor is the quantum confinement effect[42]

$$E_G(K) \cong E_G(\infty) + AK^{-2} - BK^{-1} - C \quad (1)$$

where $E_G(K)$ is the band gap of a particle with a dimensionless form of size K and $E_G(\infty)$ is the bulk band gap. A, B, and C are physical constants. The K^{-2} and K^{-1} terms represent the kinetic and potential energies of the electron−hole pairs or so called exciton. Other sophisticated models concerning the PL blue shift include color centers,[43] surface effect,[32b] etc. These models explained reasonably well the blue shift of either the PL or the photoabsorption (PA) but not both simultaneously. In fact, the PL and PA depend not only on the intrinsic E_G based on interatomic potential but also on the extent of electron−phonon coupling.[41d,44] A comprehensive understanding of the size and shape effect on the E_G expansion and the blue shift of the PA and PL as well as the electron−phonon coupling in ZnO nanostructures is highly desired.

When the solid size is reduced, the transverse optical (TO) and the longitudinal optical (LO) Raman phonons shift toward lower frequency (i.e., optical mode softening)[45] accompanied by generation and a blue shift of the low-frequency Raman (LFR) acoustic modes at wavenumbers from a few to a few tens of cm^{-1} (i.e., acoustic mode stiffening).[26c−e] Generally, the size-dependent Raman shifts follow the relationship[46]

$$\omega(K) - \omega(\infty) = D/K^n \quad (2)$$

where D and n are adjustable parameters. For the TO and LO modes softening $D < 0$; for the LFR acoustic stiffening $D > 0$. The LFR mode disappears for the infinite large crystal, $\omega(\infty) = 0$. Although eq 2 could fit the measured size trends numerically, the underlying mechanism behind the Raman shift of nanostructures remains undetermined.

Model descriptions of the Raman shift of nanostructures have been reported mainly from the perspective of phonon scattering. For the size-induced acoustic phonon hardening, Yadav et al.[26c] fitted their experimental results using Lamb's theory[47] which predicts the vibrational frequencies of a homogeneous elastic body in spherical shape. Their results show that the observed LFR scattering originates from the spherical and quadrupolar vibrations of the spheroidal mode due to confinement of acoustic vibrations in nanoparticles. Combe et al.[26e] calculated the acoustic modes of ZnO nanocrystals with a model using a semiempirical potential, which takes the effects of surface relaxation and surface stress into account. They attributed the acoustic phonon hardening to the surface effect. Liang et al.[48] proposed a model for the size-induced Raman blue shift of TiO_2 by relating the frequency shift to the bond length and bond strength as a function of the entropy, latent heat of fusion, and critical temperature for solid−liquid transition. Besides these widely used models, optical mode softening is usually suggested to be activated by surface disorder[49] and explained in terms of surface stress[50] or phonon quantum confinement[51] as well as the surface chemical passivation effect.[52]

Study of the phase stability of a material is of great importance.[53] Phase transitions such as solid−liquid, solid−solid, liquid−vapor, magnetic−paramagnetic, and ferroelectric−paraelectric transitions take place when the applied temperature and pressure reach certain conditions. The critical temperature (T_C) for phase transition of the bulk is size independent, but the T_C and critical pressure (P_C) for phase transition of nanomaterials vary with the size and microstructure of the samples and voids inside the specimen.[20a] Generally, as the size decreases or shape changes from a slab to a higher dimensional shape such as a sphere, the T_C of nanocrystals decreases.[25a,54] If one retains the T_C, the P_C will have to increase when the size is reduced.[55] The size-degenerated T_C has made the low-temperature hydrothermal synthesis of nanomaterials straightforward and

dx.doi.org/10.1021/cr200428m | Chem. Rev. 2012, 112, 2833−2852

technically flexible for the shape and structure control of surface architectures.[56]

Theoretically, there are various models describing the variation of the T_C of nanostructures with their sizes.[57] Generally, all existing models can be categorized into three groups which are based on (i) classical thermodynamics,[58] (ii) average atomic cohesive energy,[59] and (iii) the amplitude of atomic vibration[60] according to Lindeman's criterion.[134,135]

1.2.2. Temperature Dependency. Experimental observations have shown that when the operating temperature drops, the Young's modulus of ZnO nanostructures increases.[35b,c,f] The thermal effect was modeled based on the third law of thermodynamics. Wachtman et al.[61] suggested an empirical equation for the temperature effect on the Young's modulus

$$Y(T) = Y_0 - b_1 T \exp(-T_0/T) \tag{3}$$

where $Y(T)$ and Y_0 are the Young's modulus at T and 0 K, respectively. b_1 and T_0 are freely adjustable parameters. This model worked well only at high temperatures where $Y(T)$ shows a linear dependence on temperature. However, below the Debye temperature, θ_D, the measured data have a nonlinear nature.[35c,62] Andersen[63] derived an alternative by introducing the Mie−Grüneisen equation

$$\begin{cases} Y = Y_0 - \dfrac{3R\gamma\delta T}{V_0} H\left(\dfrac{T}{\theta_D}\right) \\ H\left(\dfrac{T}{\theta_D}\right) = 3\left(\dfrac{T}{\theta_D}\right)^3 \displaystyle\int_0^{\theta_D} \frac{x^3}{e^x - 1}\, dx \end{cases} \tag{4}$$

with R being the ideal gas constant, γ the Grüneisen parameter, and δ the Anderson constant which is temperature independent. V_0 is the specific volume per mole of atoms at 0 K. According to Anderson, the term $b_1 T \exp(-T_0/T)$ in eq 3 is virtually the inner energy of the Debye approximation.

From the perspective of classical thermodynamics, Garai et al.[64] derived a solution for fitting the temperature dependence of the bulk modulus

$$B_T^0 = B_0^0 \exp\left[\int_{T=0}^{T} \alpha\alpha_{V_P}\, dt\right] \tag{5}$$

where superscript 0 denotes the quantities gained at 1 bar pressure, B_0^0 is the modulus at 0 K, α is a constant depending on the material, and α_{V_P} is the volume thermal expansion coefficient. The bulk modulus B correlates with Y by $Y/B = 3 \times (1 - 2\nu)$, where ν denotes the Poisson ratio which is negligibly small; therefore, $Y \approx 3B$.

Generally, the acoustic and optical phonon modes of ZnO are softened upon heating.[65] Numerous theoretical models have been developed to explain the thermally induced Raman shift, including the anharmonic phonon decay,[66] thermal expansion,[65b] anharmonic coupling,[67] and thermal perturbation.[65d,68] Among them the perturbation approach has been prominently employed, which follows the relationship[65d]

$$\omega(T) = \omega(0) + \Delta\omega_e(T) + \Delta\omega_d(T)$$

where

$$\Delta\omega_e(T) = -\omega(0)\gamma \int_0^T [\alpha_c(T) + 2\alpha_a(T)]dt$$

$$\Delta\omega_d(T) = C\left[1 + \frac{2}{\exp(\hbar\omega/kT)}\right] + D\left[1 + \frac{3}{\exp(\hbar\omega/kT) - 1} + \frac{3}{\{\exp(\hbar\omega/kT) - 1\}^2}\right] + \text{higher order terms} \tag{6}$$

where $\omega(0)$ is the Raman frequency measured at 0 K reference temperature, $\Delta\omega_e(T)$ is the contribution from the thermal expansion, and $\Delta\omega_d(T)$ is due to the anharmonic coupling of phonons of other branches. C and D are the anharmonic parameters used to fit to the measurement. α_c and α_a are the thermal expansion coefficients along the a and c axes of a wurtzite structure.

The band gap E_G of ZnO can be increased by either decreasing temperatures or increasing external pressure.[24b,35d,e,h,69] The temperature dependence of the E_G of semiconductors can be fitted with a general form proposed by Varshni[70]

$$E_G(T) = E_G(0) - \alpha T^2/(T + T_0) \tag{7}$$

where α is the absorption coefficient that can be obtained from the absorption spectrum and T_0 is a parameter for fitting the experimental result, which was found to be closely related to the Debye temperature of the investigated material.

1.2.3. Pressure Dependency. The pressure dependence of the bulk modulus and the Raman shift under applied pressure is usually described using the quadratic functions[71]

$$Q(P) = Q(0) + aP + bP^2 \tag{8}$$

where a and b are freely adjustable parameters and $Q(0)$ represents the Raman frequency or the elastic modulus under 0 Pa pressure.

1.2.4. Emerging Phenomena. In addition to the size dependency of the known properties associated with the bulk, the most surprising phenomenon[19d] emerging with the reduction of size is the ferromagnetism of the nonmagnetic ZnO semiconductor, like GaN,[72] AlN,[73] and TiO_2.[74] They become ferromagnetic at room temperature and above when they are doped with just a few percent of transition-metal cations such as Al,[75] V,[76] Cr,[77] Mn,[3,4b] Fe,[73] Co,[74b,78] or Ni.[79]

Rough ZnO surfaces also demonstrate the superhydrophobicity against being wetted.[80] ZnO nanostructures[81] or its hybrids[6a,9a] also show enhanced catalytic ability[9d,81a] that the bulk trunks do not have.

Defects have been identified to promote the magnetism in ZnO.[82] Recent progress[83] suggests that Zn contributes negligibly to the total magnetization; the high-density regions of Mn cations with a $MnO_{2-\delta}$-distorted environment, mainly allocated at the nonstoichiometric and highly defective ZnO grain boundaries dominate the ferromagnetic properties of Mn−ZnO. This phenomenon is observed in thin films and nanocrystals but not in the well-crystallized bulk. Investigation[84] of the dilute magnetism of Cr-doped ZnO and Ni-doped SnO_2 films fabricated under various conditions implied that structural defects and oxygen vacancies, indeed, largely influence the magnetism

dx.doi.org/10.1021/cr200428m | Chem. Rev. 2012, 112, 2833−2852

in those systems. Slight nitrogen substitution for oxygen can also exhibit a high Curie temperature and small coercivity. Coey et al.[82b] proposed that the ferromagnetic exchange in dilute ferromagnetic oxides and nitrides is mediated by the shallow donor electrons that form bound magnetic polarons, which overlap to create a midgap spin-split impurity band. High Curie temperatures arise only when empty minority-spin or majority-spin *d* states lay at the Fermi level in the impurity band. The magnetic moment tends to decay with a characteristic decay time of weeks or months.

The extent of superhydrophobicity has been related to the surface energy[85] and surface roughness.[86] Surface roughening promotes the hydrophobicity or the hydrophilicity of a specific material. The decay of both the magnetization and the hydrophobicity can be reversed by UV irradiation.[87] Elimination of defects by hydrogenation and filling up oxygen vacancies can degrade the ferromagnetic ordering of some specific types of compounds.

1.3. Challenges and Objectives

Although existing models can fit numerically well for the size-, temperature-, and pressure-induced change of Young's modulus, phonon frequency shift, band gap, etc., despite freely adjustable parameters being involved, the underlying physical mechanism of the size dependency and emerging properties associated with small ZnO crystals remains yet ambiguous. All the size-dependent quantities are often taken as independent one from another. It is often that one phenomenon is associated with multiple modeling arguments. On the other hand, the emerging properties such as the dilute magnetism cannot be understood in terms of the conventional superexchange or double-exchange interaction theory of magnetism in insulators nor can a carrier-mediated ferromagnetic exchange mechanism account for the magnitude of the Curie temperatures, which are well in excess of 400 K (1/30 eV). The hydrophobicity and catalytic enhancement cannot be understood in terms of the curvature-induced surface energy and roughness without examining the chemical conditions and electronic dynamics of the surface. Most importantly, a model is highly desired for unifying the unusual and versatile behaviors of ZnO in mechanical strength, thermal stability, lattice dynamics, band gap, phase stability, dilute magnetism, enhanced catalytic ability, and superhydrophobicity simultaneously. Understanding the nature and factors dominating the general trends of the size-, pressure-, and temperature-induced properties change and the physical origin of the emerging properties of ZnO is of fundamental importance to knowledge and technology advancement.

A physical model should meet the following criteria and be able to

(1) reproduce the measured trends with meaningful parameters,
(2) provide consistent insight into the physical mechanism behind observations,
(3) extract quantitative information from the measurements,
(4) correlate the seemingly irrelevant quantities and their performance under various stimuli such as size, pressure, and temperature, as pursued in the present course.

Inspired by the Ice Rule of Pauling,[88] the atomic coordination−radius correlation of Goldschmidt[89] and Pauling,[90] and the Strong Localization theory of Anderson,[91] we attended the O, N, and C surface chemisorption bond-band forming dynamics[52,92] and the size dependency of nanostructures in the mechanical, thermal, acoustic, electronic, photonic, dielectric, and magnetic properties.[21b] Exercises have led to the theories of bond−band correlation,[79,80] bond-order−length−strength (BOLS) correlation,[21b] nonbonding electron polarization (NEP),[4a,93] and local bond averaging (LBA) method,[94] as well as the technique of zone-selective photoelectron spectroscopy (ZPS) for collecting quantitative information of bonds and electrons associated with undercoordinated surface and defect atoms. On the basis of these frameworks, we have been able to determine the length, strength, compressibility, Debye temperature, elasticity, and force constant of the C−C bond in graphene using Raman spectroscopy.[95] The most striking progress made recently is the quantification of hydrogen-bond asymmetric relaxation and vibration dynamics in water and ice. We confirmed that the Coulomb repulsion between the unevenly bound bonding (∼7.0 eV) electron pair and nonbonding (∼0.035 eV) electron lone pair in the hydrogen bond dominates the anomalies of water and ice under various stimuli including pressure, temperature, and cluster size.

The objective of this work is to report our exercises and progress made in the past 5 years on the formulation, clarification, correlation, and quantification of the behavior of ZnO based on the BOLS,[21b] the NEP,[4a] and the LBA frameworks.[96] The modeling approaches implemented may complement the sophisticated models as mentioned previously to provide consistent and deeper insight into the size, shape, temperature, and pressure effects on the known bulk ZnO properties and the emerging properties associated with the undercoordinated atoms at the surfaces and defects of ZnO.

2. PRINCIPLES

2.1. Bond-Order Loss and BOLS Correlation

Termination of lattice periodicity at the surface, point defect, or grain boundaries usually results in two consequences: one is creation of the surface potential barrier and the other is the atomic bond-order loss. The coordination number (CN) of an atom on a highly convex surface is lower than that in a flat surface plane. On the other hand, the atomic CN is higher on a concave surface such as the inner side of a cavity or a hollow tube. From the atomic CN imperfection point of view, there is no substantial difference in nature among defects, surfaces, vacancies, atomic chains, atomic sheets, solid wires, hollow tubes, and nanostructures of various shapes and sizes. In line with the important conclusions via the chemical bonding theory of single-crystal growth,[97] atomic CN loss of the surface atoms is the essential cause for the size- and shape-dependent phenomena. According to Pauling[90] and Goldschmidt,[89] if the CN of an atom is reduced, the radius of the atom would shrink spontaneously. Therefore, bond-order loss shortens the remnant bonds between undercoordinated atoms, regardless of the nature of the specific chemical bond or the structural phase, even in the liquid phase.[98]

Nanomaterials have a large proportion of surface atoms with bond-order deficiency compared with the bulk counterpart. As a result, surface skin composed of three atomic layers often relaxes and reconstructs without exception,[99] which critically affects the physical and chemical properties in the skin. In order to cope with the lower coordinated systems, we developed the BOLS correlation mechanism[21b] by extending the "atomic CN−radius" correlation of Goldschmidt,[89] Pauling,[90] and Feibelman[100] to include the response of energy and electron states to bond relaxation. The key idea of the BOLS correlation is that if one bond breaks, the remaining ones of the lower

coordinated atoms become shorter and stronger. The BOLS correlation mechanism can be expressed as

$$\begin{cases} C_i = d_i/d_b = 2/\{1 + \exp[(12 - z_i)/(8z_i)]\} \\ E_i = C_i^{-m} E_b \\ E_{Bi} = z_i E_i \end{cases} \quad (9)$$

where C_i is the coefficient of bond contraction and subscripts i and b denote an atom in the ith atomic layer and in the bulk, respectively. The i is counted up to three from outermost inward.[99] z_i is the effective CN of the specific ith atom and varies with the size and curvature of a nanostructure in an empirical way, $z_1 = 4\ (1 - 0.75/K)$, $z_2 = z_1 + 2$, and $z_3 = 12$ with K being the dimensionless form of size of the nanostructure, meaning the number of atoms lined along the radius of a sphere or across the thickness of a thin film. E_i and E_b denote the binding energy per bond in the ith atomic layer and in the bulk, respectively. The index m is an indicator of the bond nature of a specific material but is not arbitrarily adjustable. The index m may also embed the electronegativity difference[36a,52] and iconicity[37b] of a compound, which determines the ease of chemical bond formation. For ZnO, the m value has been optimized to be 2.4.[101] E_{Bi} denotes the atomic cohesive energy of an atom in the ith atomic layer and is defined as the product of the atomic CN and the bond energy.

Figure 1 shows the CN dependence of the bond-contraction coefficient $C_i(z_i)$ and bond energy $E_i/E_b = C_i^{-m}$ with different m

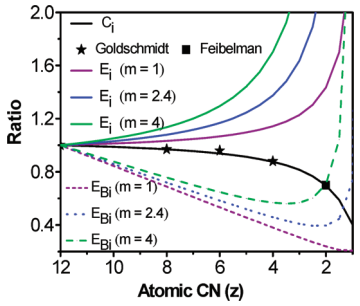

Figure 1. Atomic CN dependence of the normalized bond length $d_i/d = C_i(z_i)$, the CN and bond nature dependence of bond energy $E_i/E_b = C_i^{-m}$, and the atomic cohesive energy $E_{Bi}/E_B = z_i/z_b C_i^{-m}$. Scattered data was from Goldschmidt[89] and Feibelman.[100]

values (m = 1, 2.4, 4) as well as the relative atomic cohesive energy, $E_{Bi}/E_B = (z_i/z_b)C_i^{-m}$. The scattered data represents Goldschmidt's premise indicating that the ionic radius contracts by 12%, 4%, and 3% if the atomic CN reduces from 12 to 4, 6, and 8, respectively.[89] As a spontaneous process of CN reduction and bond contraction, the bond energy at equilibrium becomes stronger but the atomic cohesive energy drops. The down slope of C_i and the up slope of E_i/E_b in Figure 1 indicate that the bond-order loss makes the remaining bonds shorter and stronger with respect to their bulk counterparts. E_{Bi}/E_B drops because of the drop in the production of the atomic CN and the bond energy. When the CN decreases to a value of 2, E_{Bi}/E_B of ZnO increases abruptly because the sharp increase of E_i/E_b overtakes the CN reduction.

2.2. Core–Shell Configuration and LBA Method

Figure 2 presents the core–shell configuration for a grain or a nanoparticle.[102] Generally, any detectable physical quantity $Q(K)$ of a nanosolid with finite dimension K that contains N

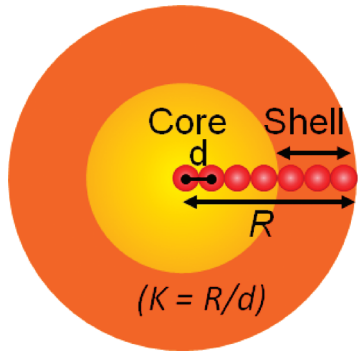

Figure 2. Illustration of the core–shell structure and dimensionless size of K. Volume ratio between the shell and the entire body will increase when the solid size is reduced.[102]

atoms can be derived based on the known $Q(\infty)$ using the core–shell configuration

$$\begin{cases} Q(K) = Nq_0 + \sum_{i\le 3} N_i(q_i - q_0) \\ \Delta_q = \dfrac{Q(K) - Q(\infty)}{Q(\infty)} = \sum_{i\le 3} \gamma_i \Delta q_i/q_0 \end{cases} \quad (10)$$

where q_0 and q_i denote the local density of Q inside the bulk and at the ith atomic layer, respectively. N_i is the number of atoms in the ith layer. $\gamma_i = \tau C_i K^{-1}$ is the volume or number ratio of the ith atomic layer to that of the entire solid. τ = 1, 2, and 3 corresponds to a nanofilm, a nanorod, and a nanosphere, respectively.

The main concept of the LBA method[101] is that we take the average of all bonds of the entire specimen so we can focus on the performance of the representative bond under various stimuli and its effect on the detectable properties of the specimen. The involvement of an interatomic bond distinguishes the performance of a solid from the isolated constituent atoms. For a given specimen, whether it is crystal, noncrystal, or with defects or impurities, the nature and total number of bonds do not change under external stimuli unless phase transition occurs. However, the length and strength of the involved bonds change in response to the applied stimuli. If the functional dependence of a detectable quantity on the bonding identities is established, one would readily know the performance of the entire specimen under external stimuli by focusing on the response of the length and strength of the representative bond for all at different sites.

The LBA approach looks for the relative change of a quantity with respect to the known bulk constant under applied stimuli. We focus merely on the performance of the local representative bonds disregarding the number and nature of all bonds which do not change. The presence of broken bonds, defects, impurities, and noncrystallinity in the bulk affects the reference bulk values rather than the nature of observations. The contribution from long-order interaction or high-order coordinates can be simplified by folding them into the bonds of a specific atom to the nearest neighbors.

2.3. Size, Pressure, and Temperature Dependency

When the solid size, operating temperature, or pressure changes, the length, $d(z_i, T, P)$, and energy, $E_i(z_i, T, P)$, of the representative bond will change simultaneously. On the basis of the LBA approach we can extend the BOLS correlation

dx.doi.org/10.1021/cr200428m | Chem. Rev. 2012, 112, 2833–2852

to temperature and pressure domains, leading to the temperature- and pressure-dependent bond length and bond energy

$$\begin{cases} d(z_i, T, P) = \prod (1 + \Delta d_i) \\ \qquad = C_i d_b \left(1 + \int_0^T \alpha_i(t)\mathrm{d}t\right)\left(1 + \int_0^P \beta_i \, \mathrm{d}p\right) \\ E(z_i, T, P) = E_0\left(1 + \sum_i \Delta E_i\right) \\ \qquad = E_0\left[1 + (C_i^{-m} - 1) + \dfrac{\Delta E_T + \Delta E_P}{E_0}\right] \end{cases} \quad (11)$$

where $\alpha(t)$ is the thermal expansion coefficient, β_i is the compressibility, E_0 is the bond energy in the bulk at the ambient conditions, and ΔE_T and ΔE_P are the energy perturbation over all the surface layers caused by the applied temperature and pressure. Figure 3a shows the pressure dependence of the Zn−O bond

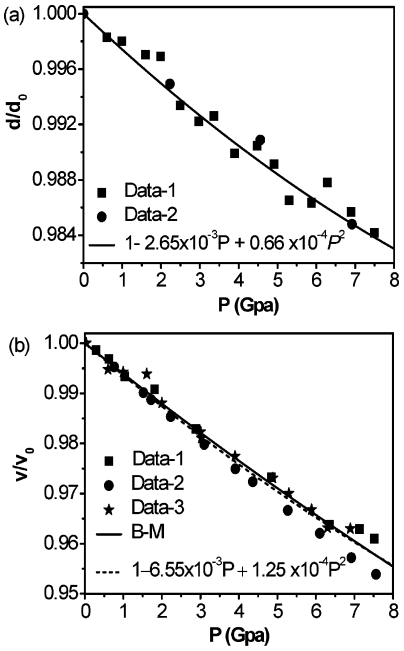

Figure 3. Fitting to the experimental data for *P*-dependent (a) bond length using the polynomial form[103] and (b) volume[103,104] of ZnO with derivatives of the linear and volume compressibility with nonlinear contributions.

length $d(P)/d(0)$ of ZnO. By fitting the experimental data with the polynomial,[103] the coefficient of linear compressibility is $\beta_i = -2.65 \times 10^{-3}$ GPa^{-1} and the nonlinear contribution $\beta_i' = 0.66 \times 10^{-4}$ G Pa^{-2}.

The ΔE_P is the pressure perturbation of energy, which can be expressed as[105]

$$\Delta E_P = -\int_{V_0}^{V} p(v)\mathrm{d}v = \int_0^P v \, \mathrm{d}p - VP$$

$$(\text{from the relationship: } d(vp) = v \, \mathrm{d}p + p \, \mathrm{d}v) \quad (12)$$

where V and P are correlated with the Birch−Mürnaghan (BM) equation of states[106]

$$p(x) = \frac{3B_0}{2}(x^{-7/3} - x^{-5/3})\left\{1 + \frac{3}{4}(B'_0 - 4)(x^{-2/3} - 1)\right\} \quad (13)$$

where V_0 is the volume of the unit cell under standard reference conditions, $V_0 \approx 48$ Å^3 for ZnO, $x = V/V_0$ is the volume ratio of the unit cell upon the cell being compressed, B_0 is the static bulk modulus, and B_0' is the first-order pressure derivative of the B_0.[103b] Figure 3b presents the V/V_0−P curve with the B−M equation and the match of the experimental results of ZnO[103,104] with an optimal polynomial form of $V/V_0 = 1 + \beta p + \beta' p^2 = 1 - (6.55 \times 10^{-3})p + (1.25 \times 10^{-4})p^2$. Using the relationship of $x = V/V_0 = 1 - \beta p + \beta' p^2$ one finds

$$\begin{cases} \Delta E_P = -\int_{V_0}^{V} p(v)\mathrm{d}v = -V_0 \int_1^x p(x)\mathrm{d}x \\ \qquad = V_0 P^2\left(\frac{1}{2}\beta - \frac{2}{3}\beta' P\right) \\ x(P) = V/V_0 = 1 - \beta P + \beta' P^2; \ \dfrac{\mathrm{d}x}{\mathrm{d}p} = -\beta + 2\beta' P \end{cases}$$

The integration area in Figure 4 shows the energy stored into the crystal that enhances the bond energy under the conditions of bond number conservation.[105]

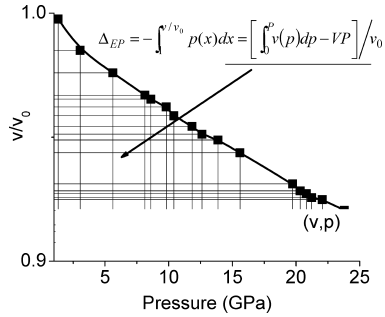

Figure 4. Schematic illustration of the pressure-enhanced bond energy.

According to the Debye approximation, temperature elevation weakens the bond energy ΔE_T in the form of

$$\begin{aligned} \Delta E_T &= \int_0^T \eta_1(T)\mathrm{d}t = \int_0^T \frac{C_V(T/\theta_D)}{z}\,\mathrm{d}t \\ &= \int_0^T \int_0^{\theta_D/T} \frac{9R}{z}\left(\frac{T}{\theta_D}\right)\frac{x^4 \exp(x)}{(e^x - 1)^2}\,\mathrm{d}x\,\mathrm{d}t \\ &= \frac{9RT}{z}\left(\frac{T}{\theta_D}\right)^3 \int_0^{\theta_D/T} \frac{x^3}{e^x - 1}\,\mathrm{d}x \end{aligned} \quad (14)$$

where $\eta_1(T = C_V/z)$ is the specific heat per bond that is assumed to follow the Debye approximation $C_V(T/\theta_D)$ and approaches a constant value of $3R$ (R is the ideal gas constant) at high temperature.

Figure 5 illustrates the reduced Debye specific heat C_V (in units of gas constant R) and its integration with respect to temperature T (or the termed specific internal energy, $U(T/\theta_D)$). At $T > \theta_D$, integration of the specific heat or specific internal energy depends linearly on T. At low temperatures, on the other hand, the integration shows nonlinearity with respect to temperature in a T^4 manner.

2.4. *K*, *P*, and *T* Coupling Effect

The coupling effect of pressure, temperature, and size on the cohesive energy of nanocrystals can be integrated based on the superposition principle of energy. External stimuli such as pressure and temperature can be taken as perturbations to the Hamiltonian. Following this consideration, the cohesive

dx.doi.org/10.1021/cr200428m | *Chem. Rev.* 2012, 112, 2833−2852

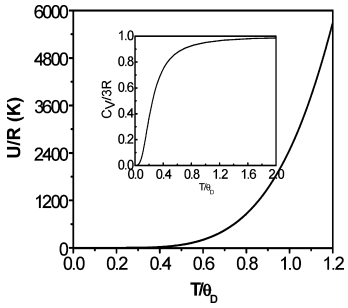

Figure 5. Debye approximation of the specific heat (C_V) (inset) and the internal energy $U(T/\theta_D)$.

energy of a spherical nanoparticle under the condition of coupling stimuli of pressure and temperature is given by

$$E_{coh}(K, P, T) = z_b E_b\left(N - \sum_{i\leq 3} N_i\right) + \sum_{i\leq 3} N_i z_i E_i$$

with

$$\begin{cases} E_i = E_{i0} + \Delta E_i^P + \Delta E_i^T = C_i^{-m} E_{b0} + \Delta E_i^P + \Delta E_i^T \\ E_b = E_{b0} + \Delta E_b^P + \Delta E_b^T \end{cases} \quad (15)$$

where E_{i0} and E_{b0} are the cohesive energy at the specific ith layer and bulk site without the external stimuli.

From the above discussion we can obtain the size-, temperature-, and pressure-dependent cohesive energy[107]

$$E_{coh}(K, P, T) = z_b\left(E_{b0} + \Delta E_b^P + \Delta E_b^T\right)\left(N - \sum_{i\leq 3} N_i\right) + \sum_{i\leq 3} N_i z_i\left(E_{i0} + \Delta E_i^P + \Delta E_i^T\right)$$

$$\frac{E_{coh}(K, P, T)}{E_{coh}(\infty, 0, 0)} = \left[1 + \sum_{i\leq 3} \gamma_i (z_{ib} C_i^{-m} - 1)\right] + \frac{\Delta E_b^P + \Delta E_b^T}{E_{b0}} \left[1 + \sum_{i\leq 3} \gamma_i \left(z_{ib} \frac{\Delta E_i^P + \Delta E_i^T}{\Delta E_b^P + \Delta E_b^T} - 1\right)\right] \quad (16)$$

If more coupling parameters are considered, x (= P, T, etc), the cohesive energy can be generalized as

$$\frac{\Delta E_{coh}(K, P, T)}{E_{coh}(\infty, 0, 0)} = \frac{\sum_x \Delta E_b^x}{E_{b0}} + \sum_{i\leq 3} \gamma_i \left[z_{ib}\left(\frac{\sum_x \Delta E_i^x}{E_{b0}} + C_i^{-m}\right) - 2\right] \quad (17)$$

The first part represents the coupling effect on the atomic cohesive energy in the bulk and the second part the joint effect in the surface skin summing over the outermost three atomic layers.

2.5. Correlation of Y, E_G, $\Delta\omega$, and T_m

All detectable physical properties of a solid are in fact correlated by the interatomic interaction and the associated electron distribution in both the energy and the real spaces. Therefore, it is essential to consider the detectable quantities from the perspective of bond and nonbond geometry, formation, dissociation, relaxation, vibration, and associated energetics and dynamics of charge repopulation, polarization, densification and localization. As demonstrated subsequently, the elastic modulus, band gap, Raman shift, and critical temperature for phase transition are all correlated to the bond order, length, and strength disregarding processes such as phonon scattering[21b]

$$\left.\begin{matrix} Y(z) \\ E_G(z) \\ \Delta\omega(z) \\ T_C(z) \end{matrix}\right\} \propto \begin{cases} E_z/d_z{}^3 & \text{(elastic modulus)} \\ E_z & \text{(band gap)} \\ z/d_z(E_z/\mu)^{1/2} & \text{(Raman shift)} \\ zE_z & \text{(critical temperature)} \end{cases} \quad (18)$$

It is seen that the elastic modulus and Raman shift are correlated by $(Yd)^{1/2}/\Delta\omega \equiv 1$ for the same material with μ being the reduced mass of a vibrating dimer. Yd is the stiffness. If one measured the trend of stiffness as a function of any stimulus, one would know the rest consequently without the need of further measurements.

3. SIZE DEPENDENCY

3.1. Elasticity

By definition, the stress σ and Young's modulus of a specimen can be derived as[101]

$$\left.\begin{matrix} \sigma = \left.\frac{\partial u(r)}{\partial V}\right|_{r\neq d} \\ Y \approx 3B = V\frac{\partial P}{\partial V} = V\left.\frac{\partial^2 u(r)}{\partial V^2}\right|_{r=d} \end{matrix}\right\} \propto \begin{cases} u(r)/r^3 & \text{(stress)} \\ E_z/d^3 & \text{(elastic modulus)} \end{cases} \quad (19)$$

where $u(r)$ is the pairing potential and V the volume. The relation between the elastic modulus and the bulk modulus is $Y \approx 3B$ if the Poisson ratio is neglected. Equation 19 indicates that the stress corresponds to the first-order differentiation of the crystal potential with respect to volume at any state of nonequilibrium. Meanwhile, the elastic modulus is the second-order differentiation of the binding energy at equilibrium with respect to volume. Both are proportional to the binding energy per unit volume at nonequilibrium for the former and equilibrium for the latter. Hence, the elastic modulus and surface stress share the same dimensionality and the same functional dependence on bonding identities. The yield stress and elastic modulus are correlated by $\sigma \approx \varepsilon B$, where ε is the specific strain at nonequilibrium.[108] The electronegativity, which determines the mechanical properties of a specimen,[36b,109] is embedded in the bond energy and the m value in the equation. For a nanosolid of V with a characteristic size K, the modulus can be expressed using the core−shell configuration

$$Y(K) = Vy_0 + \sum V_i(y_i - y_0) \quad (20)$$

where y_0 and y_i correspond to the local Young's modulus inside the bulk and in the ith atomic layer, respectively. V_i is the volume of the ith atomic shell. Thus, we can obtain a general

dx.doi.org/10.1021/cr200428m | Chem. Rev. 2012, 112, 2833−2852

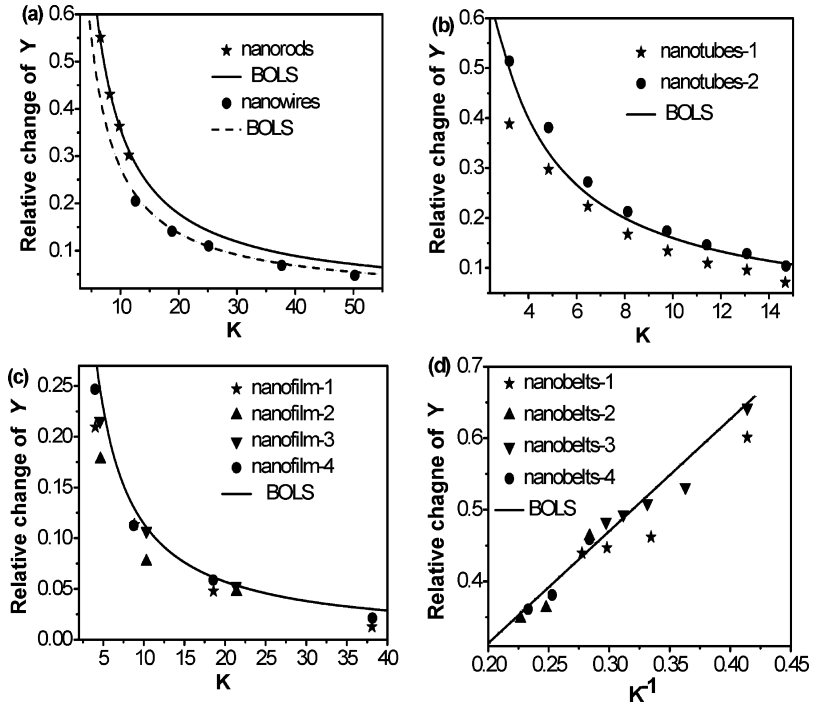

Figure 6. Theoretical (solid lines) reproduction of the computed and measured (scattered datum) Young's modulus for ZnO (a) nanowires and nanorods,[23e,54c] (b) nanotubes,[23d] (c) nanofilms,[23c,f] and (d) nanobelts[38a] as a function of size K.

form for the size dependence of the relative change of the Young's modulus with respect to the standard bulk value

$$\frac{\Delta Y(K)}{Y(\infty)} = \sum_{i\leq 3} \gamma_i \left(C_i^{-(m+3)} - 1 \right) = \tau K^{-1} \sum_{i\leq 3} C_i \left(C_i^{-(m+3)} - 1 \right) = \tau K^{-1} \Delta_Y \tag{21}$$

Equaling the predicted and the measured size dependence, $\Delta Y(K)/Y = BK^{-1}$, we see $B = \tau Y(\infty)\Delta_Y$ is the slope of the linear dependence of the elastic modulus on K^{-1}. In the numerical calculations, we plot the measured Y–K^{-1} curve to find $Y(\infty)$ as the intercept and B as the slope of the Y–K^{-1} line. The known $Y(\infty)$ = 140 GPa is the reference. C_1 = 0.8756, C_2 = 0.9376, and bond length d_0 = 0.199 nm[110] are the input parameters for calculations. It is noteworthy that $\Delta Y(\infty)/Y(\infty) \equiv 0$ in the data processing. Using the equation $B = \tau Y(\infty)\Delta_Y$ we can calculate the values of Δ_Y and hence determine the m value.

Figure 6 shows the theoretical match to the measured size dependence of the relative change of $Y(K)$ for ZnO nanowires, nanorods,[23e,54c] nanotubes,[23d] and nanofilms.[23c,54c] Only the outermost three atomic layers are considered for ZnO nanowires, nanorods, and nanofilms, but for ZnO nanotubes the contribution of both the outer and the inner shells should be included.

3.2. Band Gap

According to band theory, the Hamiltonian of an electron inside a solid can be expressed as

$$\hat{H} = \hat{H}_0 + \hat{H}' = \frac{-\hbar^2\nabla^2}{2m} + V_{\text{atom}}(r) + V_{\text{atom}}(r + R_C) \tag{22}$$

where $V_{\text{atom}}(r)$ is the intra-atomic trapping potential of an isolated atom and $\hat{H}' = V_{\text{atom}}(r) + V_{\text{atom}}(r + R_C)$ is the periodic potential of the crystal, i.e., the crystal potential. R_C is the lattice constant. According to the nearly free-electron approximation, E_G originates from the crystal potential; the width of the gap is simply twice the first Fourier coefficient of the crystal potential which is proportional to the mean cohesive energy per bond $\langle E_b \rangle$.

With a given set of Bloch wave functions $|\varphi(k, r)\rangle$ under equilibrium conditions, the interatomic potential $V_{\text{cry}}(r)$ determines the intrinsic E_G, which has little to do with the density or energy of the excitons that dictate the quantum confinement effect. Therefore, any perturbation to the V_{cry} $(r = d) \propto E_b$ will modify the E_G if the $|\varphi(k, r)\rangle$ changes insignificantly with solid size.

According to the BOLS correlation, the crystal potential and associated E_G of a nanostructure undergo a perturbation, Δ_K[21b]

$$\begin{cases} V_{\text{cry}}(K) = V_{\text{cry}}(\infty)(1 + \Delta_K) \\ \Delta_K = \dfrac{E_G(K) - E_G(\infty)}{E_G(\infty)} = \displaystyle\sum_{i\leq 3} \gamma_i (c_i^{-m} - 1) \end{cases} \tag{23}$$

The intrinsic E_G is often confused with the optical band gap detected as E_{PL} or E_{PA}. In fact, E_{PL} or E_{PA} does not equal to the intrinsic E_G because of the involvement of the electron–phonon coupling effect or the Stokes shift W. In the process of PA, an electron absorbs energy $E_{PA} = E_G + W$ and is excited from the ground to the excited state with a hole created in the ground state;[44] the excited electron then undergoes a thermalization and relaxes to the minimum of the excited state and eventually transmits to the ground state to recombine with the hole. This PL process emits a photon with energy $E_{PL} = E_G - W$. The W corresponds to the Stoke shift of the electron–phonon coupling. The Stoke shift at the ith atomic site follows the relation

dx.doi.org/10.1021/cr200428m | Chem. Rev. 2012, 112, 2833–2852

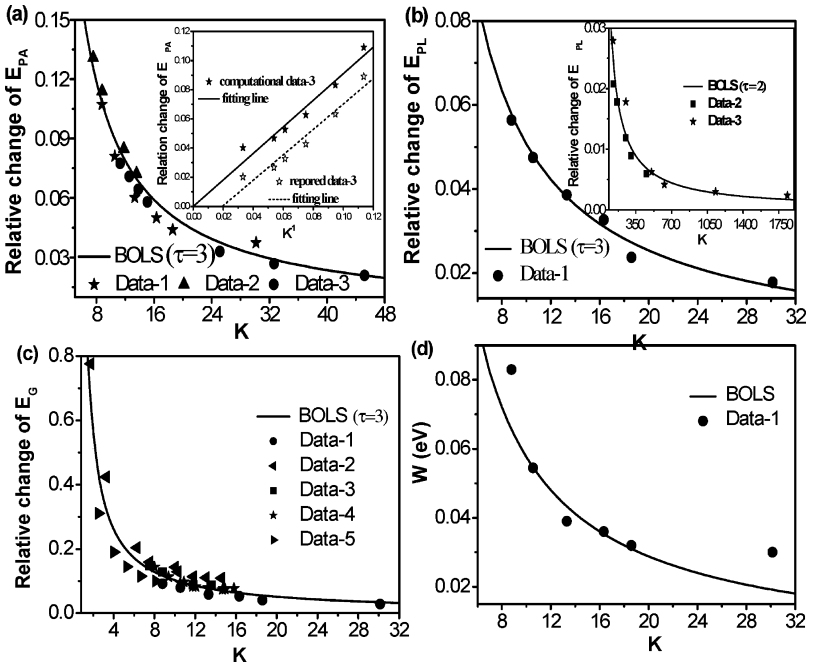

Figure 7. BOLS reproduction of the measured size dependence of (a) E_{PA} with Data 1−3 from refs 24a, 31a, and 31b. (Inset) Offset to fit $\Delta E_{PA}/E_{PA} \equiv 0$. (b) E_{PL} with Data 1−3 from refs 24a, 32c, and 114. (c) E_G with Data 1−5 from refs24a, 24c, 31a, and 32a. (d) Stokes shift $W = (E_{PL} - E_{PA})/2$ with data from ref 24a.

$W_i = Fd_i^{-2}$ with F being a constant. Counting in the surface bond contributions, the size-induced E_{PA} and E_{PL} changes can be expressed as[41d,44]

$$\left.\begin{matrix}\dfrac{\Delta E_{PA}(K)}{E_{PA}(\infty)} \\ \dfrac{\Delta E_{PL}(K)}{E_{PL}(\infty)}\end{matrix}\right\} = \frac{\Delta E_G(K) \pm \Delta W(K)}{E_G(\infty) \pm W(\infty)}$$
$$\cong \tau K^{-1} \sum_{i\le 3} C_i\left[(C_i^{-m} - 1) \pm A\left(C_i^{-2} - 1\right)\right]$$
$$= \frac{\tau\Delta_{\pm}}{K} \qquad (24)$$

where $A = F/[E_G(\infty)d_0^2]$ is a constant, and $W(\infty)/E(\infty) \approx 0$ because $W(\infty) \approx 0.01$ eV is negligibly small.[111] The first term represents the relative change of the intrinsic E_G originated from the Hamiltonian perturbation, and the second term represents the relative change of the Stokes shift due to electron−phonon coupling. If $C_i = 1$, neither E_G expansion nor PA or PL blue shift will happen. It can be derived that $E_G = (E_{PL} + E_{PA})/2$ and $W = (E_{PA} - E_{PL})/2$. The size trends of both E_G and W can thus be determined by measuring the size dependence of E_{PL} and E_{PA}. One can also measure the intrinsic E_G as the separation between the occupied and the unoccupied density of states of the specimen directly using scanning tunneling spectroscopy.[112]

Generally, the measured size trends of E_G, E_{PL}, and E_{PA} follow the linear dependence of the inverse size

$$E_x(K) = \begin{cases} E_x(\infty)(1 + \tau\Delta_x K^{-1}) & \text{(BOLS theory)} \\ E_x(\infty)(1 + C_x K^{-1}) & \text{(experiment)} \end{cases} \qquad (25)$$

where E_x represents E_G, E_{PL}, or E_{PA}. Equaling the measurement and the BOLS prediction allows one to determine the m and $E_x(\infty)$ values if they are unknown. The slope $C_x = \tau\Delta_x$. In the fitting process, $E_G(\infty) \approx E_{PL}(\infty) \approx E_{PA}(\infty) \approx 3.32$ eV were used.[31a,111b] A calibration of the measured data was conducted to satisfy the relation $\Delta E_x(\infty)/E_x(\infty) \equiv 0$ [Figure 7a inset].

Combining the PL and the PA shift in eq 24 we can also obtain $A = (\Delta_+ - \Delta_-)[2\sum_{i\le 3} C_i (C_i^{-2} - 1)]^{-1} = (C_{PA} - C_{PL})[2\tau\sum_{i\le 3} C_i (C_i^{-2} - 1)]^{-1} = 0.15$ with $\tau = 3$ for a spherical dot. The slopes were derived as $C_{PA} = 0.88$ and $C_{PL} = 0.50$. Compared with the A values for Si ($A = 0.91$) and Ge ($A = 4.26$),[44,111a] ZnO exhibits a much weaker effect on electron−phonon coupling. This difference arises from the fact that the Bohr exciton radius (about 2 nm) of ZnO is smaller than that of Si (4.9 nm) and Ge (24.3 nm).[32c] The smaller exciton radius results in a decrease in the oscillator strength of the transitions.[111a] Figure 7 shows a reproduction of the experimentally and computationally observed size dependence of the E_{PA}, E_{PL}, and E_G blue shift for different nanostructured ZnO with $m = 2.48$.[113] Exceedingly good agreement between predictions and measurements indicates that the impact of broken-bond-induced quantum entrapment and the associated electron−phonon coupling at the surface of skin depth dictates the E_G expansion.

3.3. Raman Shift

Instead of focusing on the Raman scattering process, we emphasize that the solution to the Hamiltonian of a vibration system is a Fourier series with multiple terms of frequencies being folds of that of the primary mode. Any perturbation to the Hamiltonian such as the interlayer van der Waals force, dipole−dipole interaction, or nonlinear effect may cause the folded frequencies to deviate from the ideal values, as observed from carbon allotropes.[115] On the other hand, the size, applied pressure, and temperature variation can modulate the length and energy of the involved bonds or their representative and

dx.doi.org/10.1021/cr200428m | Chem. Rev. 2012, 112, 2833−2852

hence the phonon frequencies in terms of bond relaxation and vibration.[95]

Generally, one can measure the Raman resonance frequency as $\omega_x = \omega_{x0} + \Delta\omega_x$, where ω_{x0} is the reference point from which the Raman shift $\Delta\omega_x$ proceeds under the applied stimuli. ω_{x0} may vary with the frequency of the incident radiation and substrate conditions but not the nature and the trends induced by the applied stimuli. By expanding the interatomic potential $u(r)$ in a Taylor series at its equilibrium and considering the effective atomic z, we can derive the vibration frequency shift of the harmonic system

$$\begin{aligned} u(r) &= \sum_{n=0} \left(\frac{d^n u(r)}{n! dr^n}\right)_{r=d_z} (r - d_z)^n \\ &\cong E_z + 0 + \left.\frac{d^2 u(r)}{2! dr^2}\right|_{r=d_z} (r - d_z)^2 + 0\left((r - d_z)^{n\geq 3}\right)... \\ &= E_z + \frac{\mu\omega^2 (r - d_z)^2}{2} + 0\left((r - d_z)^{n\geq 3}\right)... \end{aligned}$$

From the dimensionality analysis, the term $(\partial u(r))/(\partial r^2)|_{r=d}$ is proportional to $E_z^{1/2}/d_z$. The $E_z^{1/2}/d_z \cong (Y_z d_z)^{1/2}; (Y_z \approx E_z/d_z^3)$ is right the square root of the stiffness being the product of the Young's modulus and the bond length.[21b] Therefore, the Raman shift reflects the stiffness of a specific bond that is under stretching or bending.

Equaling the vibration energy to the third term in the Taylor series and omitting the higher order contributions we have

$$\frac{1}{2}\mu(\Delta\omega)^2 x^2 \cong \frac{1}{2}\left.\frac{\partial u(r)}{\partial r^2}\right|_{r=d} x^2 \propto \frac{1}{2}\frac{E_z}{d^2}x^2$$

At the first-order approximation, the lattice vibration frequency shift $\Delta\omega$ depends functionally on the order z, length d_z, and energy E_z of the representative bond for the entire specimen, and the reduced mass of the dimer atoms of the representative bond with $\mu = m_1 m_2/(m_1 + m_2)$

$$\begin{aligned} \Delta\omega_x(z, d_z, E_z, \mu) &= \omega_x(z, d_z, E_z, \mu) - \omega_x(1, d_b, E_b, \mu) \\ &= \Delta\omega = \sqrt{\left.\frac{d^2 u(r)}{\mu dr^2}\right|_{r=d_z}} \propto \frac{z}{d_z}\left(\frac{E_z}{\mu}\right)^{1/2} \end{aligned} \quad (26)$$

and hence

$$\Delta_\omega = \frac{\omega(K) - \omega(\infty)}{\omega(\infty) - \omega(1)} = \tau K^{-1} \sum_{i\leq 3} C_i\left(z_{ib} C_i^{-(m/2+1)} - 1\right) \quad (27)$$

where $\omega(1)$ is the vibration frequency of an isolated dimer, which is the reference point for the optical red shift upon nanosolid and bulk formation. One can measure $\omega(\infty)$ and $\omega(K)$ experimentally but not the $\omega(1)$. With the known m value derived from measurement of mentioned quantities, one can determine $\omega(1)$ and the bulk shift $\omega(\infty) - \omega(1)$ by matching the measured data to the BOLS theoretical predictions

$$\omega(K) - \omega(\infty) = \begin{cases} DK^{-1} & \text{(measurement)} \\ \Delta_\omega[\omega(\infty) - \omega(1)] & \text{(BOLS theory)} \end{cases} \quad (28)$$

Hence, the frequency shift of the dimer bond vibration to the bulk value, $\omega(\infty) - \omega(1) \equiv -D/(\Delta_\omega K)$, can be obtained. The matching of the prediction to the measurement indicates that $n = 1$ because $\Delta_K \propto K^{-1}$. In the theoretical calculations we take the known $m = 2.4$ and the $\omega(\infty)$ of 1LO mode and 2LO mode are 585 and 1165 cm^{-1}, respectively.[45a]

Figure 8a shows the match between the BOLS predictions to the measured red shift of the primary (LO) and the secondary

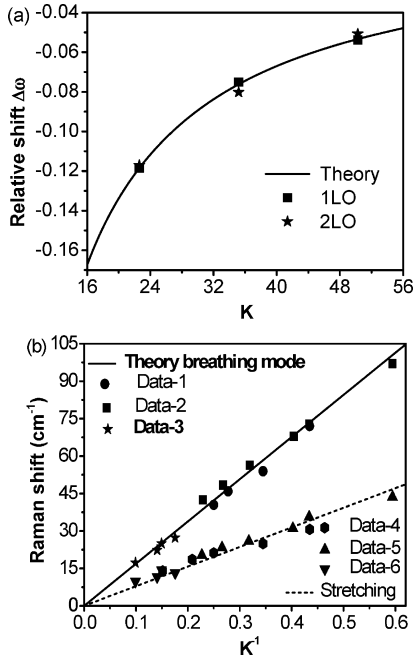

Figure 8. BOLS reproduction of the measured (scattered data) (a) optical phonon modes[45a] (1LO mode, 2LO mode) red shift of ZnO nanoparticles. (b) Fitting of the measured [46, 47, 48] size-dependent LFR frequency (breathing and stretching modes) of ZnO nanoparticles.[26c−e]

(2LO) optical phonon modes of ZnO nanoparticles.[45a] The derived $\omega(1)$ for the LO is 493 cm^{-1}, and that for the 2LO is 1019.4 cm^{-1}. Figure 8b shows the best fit to the size-dependent LFR frequency of ZnO nanoparticles, corresponding to the stretching and bending vibration with slopes of 168.97 and 78.52 cm^{-1}. The zero interception at the vertical axis indicates that when K increases to infinity the LFR peaks disappear, which confirms that the LFR modes and their blue shift are originated from interaction between nanoparticles.

3.4. Critical Temperature of Melting

In order to achieve phase transition, a certain temperature has to be reached so that all bonds can be rearranged. The thermal energy required to dissociate an atom from a solid equals the cohesive energy that is the product of atomic CN and bond energy. According to Lindeman's criterion,[116] the melting temperature of a material is proportional to its cohesive energy, $T_C = \alpha E_{coh}$, where α is a coefficient. On the basis of the same

dx.doi.org/10.1021/cr200428m | Chem. Rev. 2012, 112, 2833−2852

criterion, the BOLS theory correlates the size dependency of the melting point T_C of nanostructures to the solid size, shape, bond length, nature, and energy in the form[57]

$$\frac{\Delta T_C(K)}{T_C(\infty)} = \frac{\Delta E_{coh}(K)}{E_{coh}(\infty)} = \tau K^{-1} \sum_{i\le 3} C_i(z_{ib}C_i^{-m} - 1) = \tau K^{-1}\Delta_C = BK^{-1} \quad (29)$$

Taking the known $T_C(\infty) = 2248$ K for ZnO and the derived m and C_i values, the $T_C(K)$ for ZnO can be evaluated. Figure 9 shows theoretical reproduction of the measured size dependence of T_C for ZnO nanowires with circular and square cross sections.[25a] It can be observed that the change in T_C for ZnO nanowires with a square cross-section is larger than that of the circular cross-section. The surface to volume ratio of the square cross-section is larger than that of the circular one. The ratio between them is $8/2\pi > 1$. The melting temperature for ZnO nanostructures decreases with size because the integrated cohesive energy for surface atoms is much lower than that of the bulk due to the reduced CN and overall decrease in cohesive energy. Therefore, it is clear that depression of the melting points for nanostructures is dominated by the outermost three atomic layers, while atoms in the core interior remain their bulk nature. At $K = 8$ ($D \approx 3.2$ nm) the melting point (T_m) drops by 60% from 2248 to 900 K at which the superplasticity may happen because of the reduced separation of ($T_m - T$) and the self-heating during stretching.[117]

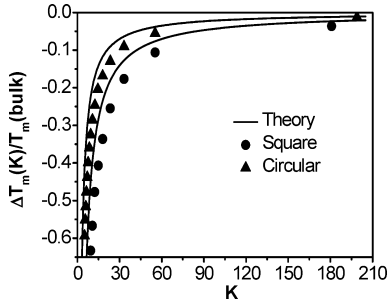

Figure 9. Theoretical (solid lines) reproduction of the measured (scattered datum) size dependence of the melting temperature (solid–liquid) for ZnO nanowires of different cross-sectional shapes.[25a]

4. TEMPERATURE DEPENDENCY

4.1. Elasticity

According to the temperature- and pressure-dependent bond length and bond energy derived in section 2.3, we can obtain the analytical expression for the T-dependent Young's modulus for a fixed size of ZnO

$$\frac{Y(T)}{Y(0)} = \left(1 + \frac{\Delta E_T}{E_0}\right)\left(1 - \int_0^T \alpha(t)dt\right)^{-3} \quad (30)$$

With the ΔE_T given in section 2.3, we can predict the T dependence of Y. In the numerical calculations, we adopt the known Debye temperature ($\theta_D = 310$ K)[104] and thermal expansion coefficient $\alpha(t)$ for ZnO as input. In ZnO crystal with wurtzite structure, $\alpha(t)$ is anisotropic. The principal values of $\alpha(t)$ in the hexagonal structures are those perpendicular and parallel to the c axis, $\alpha_a = 6.05 \times 10^{-6} + (2.2 \times 10^{-9})t + (2.29 \times 10^{-12})t^2$ and $\alpha_c = 3.35 \times 10^{-6} + (2.38 \times 10^{-9})t + (9.24 \times 10^{-14})t^2$,[118] respectively. The effective $\alpha(t)$ is an average of $(2\alpha_c + \alpha_c)/3$.[119] On the other hand, for $T > \theta_D$, C_V approaches a constant values, and $U(T/\theta_D)$ has an approximately linear dependence on temperature. Hence, the relative change in Y at high temperature can be approximated as

$$\frac{Y(T)}{Y(0)} = 1 - \frac{\eta_1 T}{E_b(0)} = 1 - A \times T \quad (31)$$

Experimentally, the slope A can be easily determined by linear fitting to the change in Y versus T at the high-temperature range of the curve. Using the relation $A_{exp} \approx A = \eta_1/E_b(0)$ with $\eta_1 \equiv 3R/z$, the binding energy per bond E_b can be estimated as 0.75 eV for ZnO and then is used as an initial input to refine the fitting to the experimental data in the whole temperature range by including the contribution of the nonlinear lattice thermal expansion. Figure 10a shows the theoretical match to the measured temperature dependence of the $Y(T)$ for ZnO at atmospheric pressure.

4.2. Band Gap

According to the LBA framework, the temperature effect on E_G follows

$$\frac{E_G(T)}{E_G(0)} = 1 + \frac{\Delta E_T}{E_0} \quad (32)$$

Figure 10b compares the theoretical and measured temperature-dependent E_G of ZnO nanostructures with different sizes and shapes at atmospheric pressure and in the temperature range of 0–840 K.

4.3. Raman Shift

Likewise, the T dependence of the Raman shift for a fixed size is derived as[121]

$$\frac{\omega(T) - \omega(0)}{\omega(0) - \omega(0)} = \left(1 + \frac{-\Delta E_T}{E_b(0)}\right)^{1/2}\left[1 + \int_0^T \alpha(t)dt\right]^{-1} \quad (33)$$

Figure 10c shows the theoretical reproduction with the measured temperature-dependent Raman shift of E_1(LO), A_1(LO), and E_2(high) modes at atmospheric pressure with the known $\omega(\infty)$ of E_1(LO, 595 cm^{-1}), A_1(LO, 579 cm^{-1}), and E_2(high, 441.5 cm^{-1}) modes.[65b,d] Agreement between predictions and observations allows us to determine the $\omega(1)$ of E_1(LO, 510 cm^{-1}), A_1(LO, 502 cm^{-1}), and E_2(high, 380 cm^{-1}) modes.

It can be observed that the change of Y, E_G, and the Raman shift with temperature turns from nonlinear to linear as temperature is increased above $\theta_D/3$. In the low-temperature regime, the $\int_0^T \eta\, dt$ is very small as the specific heat $\eta(t)$ is proportional to T^3, which results in the small change of the concerned properties at low temperatures. The Debye temperature θ_D determines the shoulder width of the $Q(T)$ curves in general. Furthermore, the value of $1/E_{coh}(0)$ determines the slope of the linear region at high temperatures. Therefore, from formulating the temperature dependence of any quantity, we can determine the Debye temperature θ_D and the atomic cohesive energy $E_{coh}(0)$ of a specimen as unique parameters,[9c] which should be the pursuit of a thermal measurement.

4.4. Crystal Size Control by Programmed Annealing

Thermal heating has been used to control crystal synthesis, postannealing growth, and physical properties at will with unfortunately an unclear mechanism and quantitative correlations.

dx.doi.org/10.1021/cr200428m | Chem. Rev. 2012, 112, 2833–2852

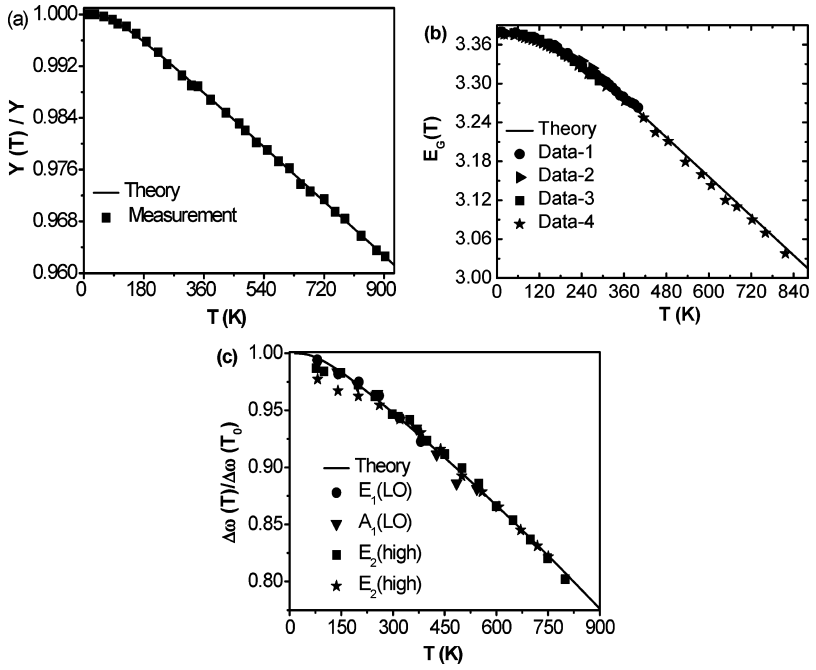

Figure 10. Theoretical (solid lines) reproduction of the measured (scattered datum) temperature dependence of (a) the Young's modulus,[35c] (b) the band gap E_G,[35d,69,120] and (c) the Raman phonons of the optical modes (E_1(LO), A_1(LO), and E_2(high))[65b,d] at atmospheric pressure for ZnO with confirmation of θ_D = 310 K and derivative of E_b = 0.75 eV per bond.

Here, we correlate the minimum critical size (K_C) with T_C based on the BOLS correlation and the atomistic thermodynamics, so that the heating temperature, sample size, and physical properties for ZnO nanocrystals can be correlated, which provides guidelines for sample growing.

The cohesive energy, E_{coh}, determines the nanoparticle size grown at a certain temperature T_C as it is directly related to the cohesive energy in a similar manner that the melting point does.[122] The size of a particle in nucleation depends on the ratio between the sintering (T_S) and the melting temperature (T_m) of the specimen, T_S/T_m.[123] When $T_S \approx 0.3T_m$, particle growth is in equilibrium and the size is stable.[124] Larger grains require higher T_S, and smaller grains needs lower T_S.[125] As a competing factor, T_m drops with grain size.[25a,126] According to eq 29, size-dependent T_m can be expressed as

$$\begin{cases} T_m(K) = T_m(\infty)(1 + \Delta_C) \\ \Delta_C = \tau K^{-1} \sum_{i\leq 3} C_i(z_i/z_b \times C_i^{-m} - 1) = K^{-1}\Delta'_C \end{cases} \quad (34)$$

In the process of sintering, any particle larger than K_C will be deposited as such. On the other hand, if the incident cluster size is smaller than K_C, the landing particles will melt upon deposition and will coagulate to produce clusters equal to the critical size or larger. Therefore, K_C and T_S are related to T_m in the sintering process[102,123]

$$\begin{cases} T_S = 0.3T_m(K) = 0.3T_m(\infty)(1 + K^{-1}\Delta'_C) \\ K_C = \dfrac{\Delta'_C}{T_S/[0.3T_m(\infty)] - 1} = \dfrac{|\Delta'_C|}{1 - T_S/[0.3T_m(\infty)]} \end{cases} \quad (35)$$

For the postannealing process, the as-grown particle size (K_0) and the threshold temperature (T_{th}) need to be involved. The high-energy grain boundary does not gain mobility until reaching T_{th},[127] at which grains grow upon heating to minimize the overall energy. With T_{th} and K_0 being considered, the completed expression for K_C allowed by the respective annealing temperature (T_a) becomes[102]

$$\begin{cases} T_a - T_{th} = 0.3T_m(K) = 0.3T_m(\infty)(1 + K^{-1}\Delta'_C) \\ K_C - K_0 = \dfrac{\Delta'_{coh}}{(T_a - T_{th})/[0.3T_m(\infty)] - 1} \\ \qquad = \dfrac{|\Delta'_C|}{1 - (T_a - T_{th})/[0.3T_m(\infty)]} \end{cases} \quad (36)$$

This relation formulates the relationship for the critical crystal size depending on the substrate or annealing temperature. Grain grows as T_a rises when $T_a > T_{th}$. For a given T_a, the grain radius K is hence predictable. Experimentally, K_0 and T_{th} are determined to be 50 and 573 K, respectively.

According to eq 36, grain size tuned by different T_a can be theoretically predicted as shown in Figure 11. Experimental results show good agreement with expectations, especially before the grains gain fast growth. The stable grain size increases rapidly with temperature when T_a is above 900 K. At higher T_a, although there is an increase in discrepancy between experiments and calculations, the deviation does

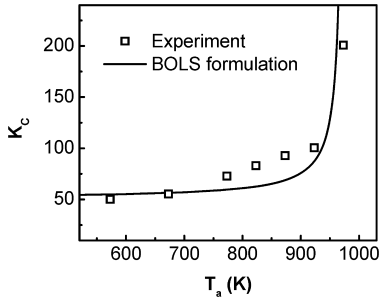

Figure 11. Comparison of the theoretically predicted K_C at various postannealing temperatures with experimentally measured results.[102]

dx.doi.org/10.1021/cr200428m | Chem. Rev. 2012, 112, 2833–2852

not have a strong effect as the grains are in the submicrometer regime and surface atoms gradually lose their hegemony. Consistency between experiment and calculation confirms the validity of BOLS theory, which can provide guidelines for controlling grain size and related properties such as band gap by programmable sintering and annealing.[102]

5. PRESSURE DEPENDENCY

5.1. Elasticity

The analytical expression for the P dependence of Y for a fix-sized ZnO follows the relationship

$$\frac{Y(P)}{Y} = \left(1 + \frac{\Delta E_P}{E_0}\right)\left(1 - \int_{0_0}^{P} \beta(p)\mathrm{d}p\right)^{-3}$$

According to this expression, the pressure dependence of the bulk modulus can be obtained with derivatives of the compressibility and binding energy density. Figure 12 shows a theoretical reproduction of the measured[35b] pressure dependence of the bulk modulus. Compared with the thermally softened ZnO Young's modulus, the pressure-induced elastic stiffening results from bond compression and bond strengthening owing to mechanical work hardening. In this calculation, we adopted the known β, β', β_d, and β_d', calculated the $B(P)$, and obtained the binding energy density (E_d) of 0.097 eV/Å^3.

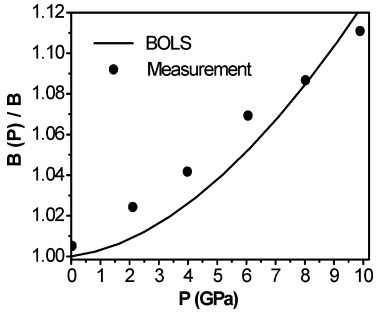

Figure 12. Theoretical reproduction of the measured[35b] pressure dependence of the bulk modulus for ZnO with derives of compressibility and binding energy density.

5.2. Band Gap

The analytical expression of the P-dependent E_G for a given ZnO is

$$\frac{E_G(P)}{E_G(0)} = 1 + \frac{\Delta E_P}{E_0} = 1 + \frac{1}{E_d}\left(\frac{1}{2}\beta P^2 - \frac{2}{3}\beta' P^3\right)$$

Figure 13a compares the predicted with the measured pressure dependence of the E_G of ZnO nanostructures at different temperature and size. Generally, the energy increases nonlinearly with pressure according to the nonlinear P–x relation. This can be ascribed to the fact that the $x = V/V_0$ of the unit cell becomes smaller upon compression.

According to the results, the temperature effect should be included but the size effect is limited when the solid size is greater than 30 nm as the surface to volume ratio is so small that it loses significance. At the same temperature, good agreement between theory and measurement evidence that pressure-induced E_G expansion in ZnO nanostructures mainly arises from pressure-induced bond strengthening. Furthermore, the multifield coupling effect indeed occurs only in the surface skin, so this effect can be omitted for larger particle size. The relation between E_G and the energy of the free exciton (E_{FX}) and its nth LO phonon replicas can be expressed as $E_{FX\text{-}n\mathrm{LO}} = E_G + 3/2 \times k_B T - n\hbar\omega_{LO}$, where k_B is the Boltzmann constant, $\hbar\omega_{LO}$ represents the LO phonon energy, and $\hbar\omega_{LO}$ = 72 meV.[35h]

Application of pressure increases the binding energy of a shallow exciton due to an increment in the electron effective mass and a reduction in the dielectric constant as E_G is increased. Besides, the energy of LO phonon also increases with pressure. However, the pressure-induced increase in exciton binding and LO phonon energies in ZnO are estimated to be much less than that of E_G.[35g,128] Therefore, the effect of pressure on exciton emission is likely originated from the E_G expansion of ZnO. According to the aforementioned discussion, we reproduce the experimental results of the pressure-dependent energy of E_{FX} with its nth LO phonon replicas measured at 70 K in ZnO nanostructures as represented in Figure 13b.

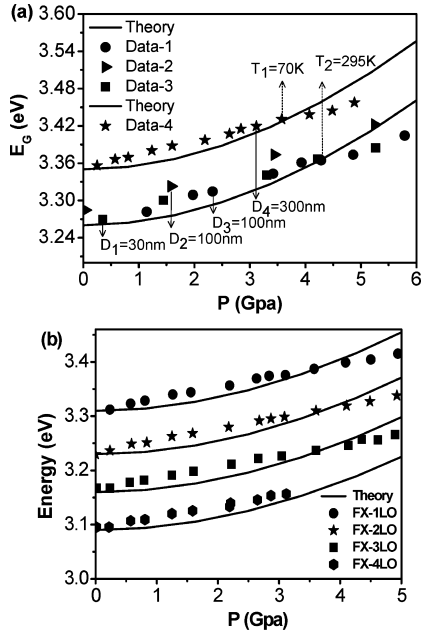

Figure 13. Theoretical (solid lines) reproduction of the measured (scattered datum) pressure dependence of (a) E_G for ZnO at the variety of sizes and temperatures,[35e,g,h,129] and the (b) measured pressure dependence of $E_{FX\text{-}n\mathrm{LO}}$ at 70 K.[35h]

5.3. Raman Shift

The analytical form for the P dependence of the Raman shift for the fix-sized ZnO is given as[128,130]

$$\frac{\omega(P) - \omega(0)}{\omega(P_0) - \omega(0)} = \left(1 + \frac{\Delta E_P}{E_b(P_0)}\right)^{1/2}\left[1 + \int_0^P \beta(p)\mathrm{d}p\right]^{-1}$$

Figure 14 presents the theoretical match with the measured pressure-dependent Raman shift of E_1(LO, 595 cm^{-1}), E_2(high, 441.5 cm^{-1}), E_1(TO, 410 cm^{-1}), A_1(TO, 379 cm^{-1}), and B_1(LO, 302 cm^{-1}) phonon modes for ZnO at room temperature.[65e,f] Agreement between predictions and experimental observations allows us to determine the $\omega(1)$ of E_1(LO, 510 cm^{-1}), E_2(high, 380 cm^{-1}), E_1(TO, 355 cm^{-1}), A_1(TO, 330 cm^{-1}), and B_1(LO, 271 cm^{-1}) modes. The change of the bond energy is dependent on the ambient temperature and

dx.doi.org/10.1021/cr200428m | Chem. Rev. 2012, 112, 2833–2852

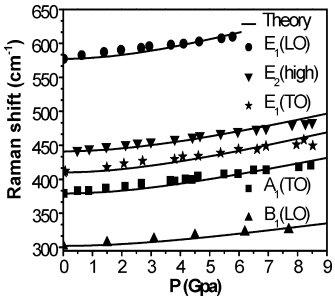

Figure 14. Theoretical (solid lines) reproduction of the measured (scattered data) pressure dependence of optical modes (E_1(LO), E_2(high), E_1(TO), A_1(TO), and B_1(LO)) for ZnO.[65e,f]

pressure. Therefore, the measured blue shift of the Raman peaks under increasing pressure results from the competition between the thermal expansion and the pressure-induced compression. Results suggest that pressure dominates the trend of change.

5.4. Pressure- and Size-Induced Solid−Solid Phase Transition

The solid−solid phase transition plays an important role in engineering design, as the structure of the nanosolid greatly affects its physical properties. Both temperature and pressure can alter the phase structure. The temperature for the solid phase transition works in a similar manner as the melting point, as shown in eq 29. If the applied pressure is increased, all of the bonds of the specimen become shorter and stronger because of the compressive force, assuming that the pressure-induced energy is equally distributed among all bonds without discrimination on the bonds in the surface skin. The pressure-induced cohesive energy increment can be represented by a summation of single bond energy change for all coordinates, i.e., $\Delta E_{coh}^{P} = z\Delta E_p$. The coupling effect of size, pressure, and temperature on the atomic cohesive energy follows

$$\frac{\Delta E_{coh}(K, p, T)}{E_{coh}(\infty, 0, 0)} = \frac{\sum_x \Delta E_b^x}{E_{b0}} + \sum_{i\le 3} \gamma_i \left[z_{ib} \left(\frac{\sum_x \Delta E_i^x}{E_{b0}} + C_i^{-m} \right) - 2 \right]$$

$$\Delta E_{coh}^{P} = -\int_{V_0}^{V} P\, dV = \frac{z}{n}\int_{0_0}^{P_C} V\, dP - V_C P_C \cong V_0 P_C \left(1 + \frac{1}{2}\beta P_C + \frac{2}{3}\beta' P_C^2 - \frac{V_C}{V_0}\right) \quad (37)$$

Extending eqs 29 and 37, we can obtain the relation of the size- and pressure-dependent phase transitions of nanostructures[105]

$$\frac{\Delta T_C(K_j, P_j)}{T_C(\infty, P_C)} = \frac{\Delta T_C(P_{Cj})}{T_C(P_{Cb})} + \frac{\Delta T_C(K_j)}{T_C(\infty)} = \frac{P_{Cj}\left(1 - \frac{1}{2}\beta P_{Cj} + \frac{2}{3}\beta' P_{Cj}^2 - \frac{V_c}{V_0}\right)}{P_{Cb}\left(1 - \frac{1}{2}\beta P_C + \frac{2}{3}\beta' P_C^2 - \frac{V_c}{V_0}\right)} - 1 + \frac{B}{K} = \delta \quad (38)$$

Equation 38 indicates that the competition between the pressure-induced overheating (T_C elevation) and the size-induced undercooling (T_C depression) dominates the measured size trends of the pressure-induced phase transition. P_{Cj} can be obtained by including boundary conditions: If the T_C values are measured to be different for all possible sizes, $\delta \neq 0$; for the phase transitions occurring at identically ambient temperature, $\delta = 0$. Thus, we obtain

$$P_{Cj} = A_j\left(1 - \frac{B}{K_j} + \delta\right) \cong P_{Cb}\left(1 - \frac{B}{K_j} + \delta\right) \quad (39)$$

with $A_j = P_{Cb}[(1 - \beta P_{Cj}/2 + 2\beta' P_{Cj}^2/3 - V_c/V_0)]/P_{Cj}(1 - \beta P_{Cj}/2 + 2\beta' P_C^2/3 - V_C/V_0) \cong P_{Cb}$

Figure 15 shows the size dependence of the critical pressure of the phase transition from the hexagonal wurtzite structure

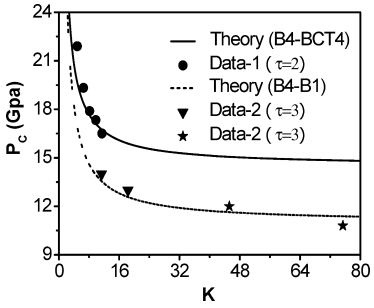

Figure 15. Theoretical reproduction of the measured size and pressure dependence of the phase transition from B4 structure to B1 structure[25e,131] and BCT4 structure[54c] of ZnO nanodots and nanowires.

(B4) to the cubic rocksalt structure (B1) and body-centered tetragonal (BCT4) structure of ZnO nanostructures. Consistency is found between predictions and the measured data, which are found in refs 25e and 131. In calculations, the input for the bulk critical pressure are 11 and 14.5 GPa for the respective phase transition at room temperature.[132]

6. DILUTE MAGNETISM, SUPERHYDROPHOBICITY, AND ENHANCED CATALYSIS

6.1. Defect and Impurity States

At sites surrounding even less-coordinated atomic vacancies or defects, the characteristics of the nonbonding lone-electron states become pronounced.[4a133] Polarization occurs to nonbonding electrons at the upper edge of the valence band, if they exist, by the densely, deeply, and locally entrapped bonding and core electrons of the undercoordinated atoms, as illustrated in Figure 16.

The following phenomena are expected to happen due to the coupling of the local bond relaxation, quantum entrapment, and the lone-electron polarization:

(1) The locally locked unpaired electron dipoles with nonzero spins will form at sites surrounding atomic vacancies, defects, adatoms, terrace edges, etc.
(2) The dipole states are readily probed as the Dirac−Fermi polarons using STM/S as high protrusions with energies at E_F.
(3) The polarized states could reduce the work function, which may enhance the catalytic ability of undercoordinated ZnO serving as a donor type catalyst, like AgPd alloy[135] and undercoordinated Rh[136] and W[137] atoms.

dx.doi.org/10.1021/cr200428m | Chem. Rev. 2012, 112, 2833−2852

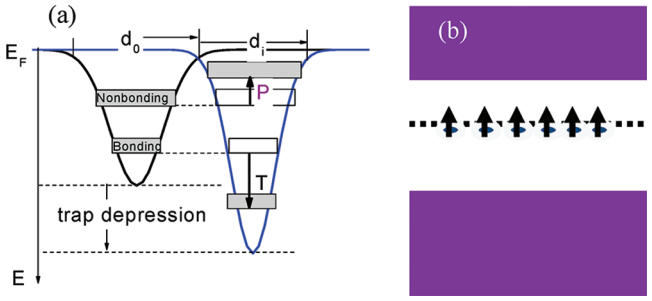

Figure 16. (a) Atomic-undercoordination-induced local bond contraction ($d_i < d_0$), and the associated quantum entrapment (T), and polarization of the nonbonding states (P) by the densely, deeply, and locally entrapped bonding and core charges.[4a] (b) Locally polarized unpaired electrons add impurity states in the midgap region, demonstrating nonzero spin each.[134] These processes modulate the Hamiltonian by crystal potential screening and splitting, which determine the charge distribution in the full span of energy.[133]

(4) The polarized lone electrons demonstrate nonzero spin values being responsible for the measured magnetism of nonmagnetic metal clusters, but their stability and intensity are subject to confirmation for practical device applications.

(5) Coulomb repulsion at the contact interfaces of such polarized media would be responsible for the superhydrophobicity of ZnO nanostructures.[80a]

XPS measurements, as shown in Figure 17, revealed that a negative Zn $2p_{3/2}$ binding energy shift of 1.2 eV happens when the ZnO crystal is reduced from 200 to 3.0 nm,[24e] which evidences the size-reduction enhanced polarization. Two kinds of ZnO defects can be generated by annealing the specimen up to 900 °C under ambient pressure of H_2 3% + Ar 97% (I) and O_2 21% + N_2 79% (II) for 24 h.[139a] Type I shows the PL energy at 2.46 eV and type II at 2.26 eV. Annealing under O_2 100% ambient pressure lowers the PL peak to 2.15 eV.[139b] Findings indicate that O passivation reduces the band gap. As the band gap is proportional to the binding energy per bond, the screening of the crystal potential by the dipoles could narrow the band gap. For both I and II types, the valence band maximum moves down and the valence band is broadened slightly as the relative intensity of the green emission to that of UV emission increases.

However, the Zn $2p_{3/2}$ core bands shift oppositely: O passivation raises the Zn $2p_{3/2}$ binding energy up, and H_2 passivation moves it deeper. These findings evidence that H passivation weakens while O passivation and size reduction enhances the surface polarization of ZnO.[4a]

It is expected that H-passivation-reduced polarization will quench the magnetism of ZnO, like the effect of hydrogen chemisorption on the magnetism of Pt nanoclusters.[140] It has been reported that the magnetization of Pt nanoparticles decreases with the increase of particle diameter or by H passivation,[141] which indicates that only atoms in the curved surface or point defect contribute to the dilute magnetism[87] and the catalytic ability of Pt.[136]

6.2. Role of Defects and Impurities

The dilute magnetism, catalytic ability enhancement, and hydrophobicity associated with the even undercoordinated defects can be unambiguously attributed to the locally locked and polarized nonbonding electrons. These nonbonding electrons include those otherwise conducting electrons in metals and the lone-electron-pair-induced dipoles in oxide and nitrides. These electrons are usually delocalized and paired exhibiting no values of spin. However, near the broken bonds, situations change entirely. These electrons will be locally pinned and polarized by the deeply and densely trapped bonding and core electrons. These locked electrons no longer contribute to conductivity because of the lowered mobility but they demonstrate measurable magnetism, hydrophobicity, and catalytic performance.[4a,86a]

In contrast to the magnetism displayed by nanoclusters of noble metals[87] and graphene nanoribbons,[4a] the diluted magnetism, catalytic ability, and superhydrophobicity displayed by nanostructured oxides result mainly from the locked dipoles due to polarization of the unpaired electrons. However, in the presence of additional O atoms or filling the oxygen vacancies, these dipoles give away the polarized electrons to form bonds with the former, which leads to a reduction of the magnetic character, being the same as the function of hydrogen surface termination. The Curie temperature higher than 400 K corresponds to the lone-pair interaction of ~0.05 eV (600 K), and the UV reversion corresponds to removal of surface contamination or dehybridization of sp orbitals, which diminishes the surface dipoles. The presence of antibonding dipoles at the open surface may correspond to and elaborate the oxygen vacancy effect as referred.

The analysis may also apply to the ferromagnets for nitrides and hexaborides, thiol-coated noble metal nanoparticles, purely organic systems, and even silicon, with a spin-split impurity band near the E_F being coincident with that generated by the unpaired dipole states as we discussed. Therefore, the locally polarized dipoles of unpaired electrons dominate the emerging

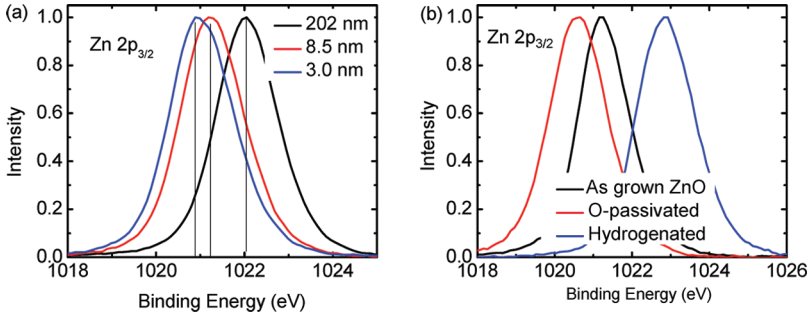

Figure 17. Normalized Zn-$2p_{3/2}$ XPS spectra showing (a) cluster size-induced polarization (upward shift) that screens in turn the crystal potential and causes the negative core level shift.[24e] This trend is opposite in direction to the core level shift of metal clusters.[138] (b) $0.21O_2 + 0.79N_2$ annealing-enhanced polarization and $0.03H_2 + 0.97Ar$ annealing annihilation of polarization and enhanced entrapment of the binding energy of Zn $2p_{3/2}$ in ZnO.[139] H passivation annihilates the surface dipoles and hence the screening effect on the crystal potential.[4a]

dx.doi.org/10.1021/cr200428m | *Chem. Rev.* 2012, 112, 2833–2852

of dilute magnetism, catalytic enhancement, and superhydrophobicity as consequences of the undercoordinated defect and curved surface atoms.

This finding may extend the models of surface energy and surface roughness for the superhydrophobicity to the bonding perspective. The higher the surface convexity or the lower the atomic CNs, the shorter and stronger the bonds, the higher the surface energy density, the lower the atomic cohesive energy, and the higher extent of polarization will be, as we demonstrated.

Caution shall be taken when one is seeking applications of the undercoordination-induced dipole magnetism. First, the stability of the magnetrons shall be considered. The binding energy of the magnetron is in the meV level; any perturbation by UV irradiation or thermal excitation may demolish them. Second, chemisorption by exposing the sample to the environment may decrease the magnetism, as the dipoles are readily annihilated by contamination at ambient conditions. Finally, the magnetic intensity depends on the total number of defects. The weak magnetism may not suffice to the sensitivity requirement of practical memory and sensing devices.

7. CONCLUDING REMARKS

We formulated, unified, clarified, and quantified the size, pressure, and temperature dependency of the elastic modulus, band gap, Raman shift, critical temperature, and correlation between the dilute magnetism, catalytic performance, and superhydrophobicity of ZnO with consistent insight into their interdependence and common origin. On the framework of the BOLS correlation, nonbonding electron polarization, and the LBA method, we presented a set of analytical expressions connecting the macroscopically detectable properties directly to the bonding identities of the ZnO and their response to the intrinsic coordination imperfection and the extrinsically applied stimuli of temperature and pressure. Theoretical reproduction of measurements revealed the following.

(1) The elastic modulus, band gap, melting point, and phonon frequency shift can be unified in terms of the nature, order, length, and energy of the representative of all bonds involved, provided that the nature and total number of bonds do not change under external stimuli unless phase transition occurs. Hence, these quantities, and beyond, are strongly correlated.

(2) The length and energy response of the representative bond to the applied stimuli of CN reduction, heating, and compressing will feedback to the measured quantities without bothering necessarily the classical thermodynamics in terms of surface energy, Gibbs free energy, entropy, or enthalpy, etc.

(3) The broken-bond-induced local strain, skin depth energy pinning, and tunable fraction of lower coordinated atoms in the surface of skin depth dominate the size dependency of various properties of ZnO. Heating elongates and weakens while compressing shortens and strengthens the representative bond and hence modulates the associated properties.

(4) The crystal size and associated properties of ZnO can be controlled by programmable annealing. Analytical formulation provides a guideline for one to design and grow materials at will with desired properties.

(5) The coupling effect of crystal size, temperature, and pressure dominates only in the skin region up to three atomic layers in depth on the materials performance such as the size- and pressure-induced phase transition.

(6) The dilute magnetism, superhydrophobicity, and enhanced catalytic performance of ZnO are correlated to the local quantum entrapment and polarization induced by the even lower coordinated atoms at the highly curved surface and defects. The localization, polarization of the unpaired, nonzero-spin, nonbonding electrons by the deeply and densely entrapped core electrons forms a locked dipole layer that prevents the surface from being wetted, and these dipoles demonstrated weak magnetism. The lowered workfunction by dipole formation may make ZnO a donor-type catalyst. Care should be taken for one to use the defect-related magnetism in practical applications as memory or sensor devices because of the limitation of thermal and chemical stability, and signal intensity.

(7) It is essential to consider the macroproperties of a solid from the perspective of bond and nonbond formation, dissociation, relaxation and vibration, and the associated energetics and dynamics of charge localization, densification, polarization, and redistribution. It is also necessary to integrate the defect, sur, and nanostructures in terms of undercoordination. It would be essentially meaningful to consider the surface skin instead of the conventional concept of surface without thickness.

(8) It is expected that the high electron emissivity and high biosensitivity of undercoordinated ZnO originate from the same origin of undercoordination-induced quantum entrapment and polarization. The nonbonding electronic energetics and dynamics and the derivatives are expected to have an important impact on conventional solid state physics and chemistry, which may form a subject area of research that is even more fascinating, promising, and rewarding.

AUTHOR INFORMATION

Corresponding Author

*E-mail: ecqsun@ntu.edu.sg.

Notes

The authors declare no competing financial interest.

Biographies

Jianwei Li received his Ph.D. degree in Condensed Matter Physics at Xiangtan University, China, in 2012. His research interests include mechanical strength, lattice dynamics, thermal stability, and optical

properties of low-dimensional semiconductor materials of ZnO in particular.

Shouzhi Ma is a Ph.D. student at Nanyang Technological University, Singapore. Her research interests are in the size effect on ferroelectric and dielectric properties of nano-oxides.

Xinjuan Liu received her Ph.D. degree at East China Normal University in 2012. Her research interests are in the size, temperature, and pressure dependence of mechanical, thermal, and vibration properties for nanomaterials, photocatalytic reduction of the metal ion, and photocatalytic degradation of organic pollutants.

Zhaofeng Zhou received her Ph.D. degree in 2009 at Xiangtan University, China. Her research interests are in low-dimensional physics and chemistry, focusing on the thermal stability and mechanical properties of nanostructures based on the bond-order–length–strength correlation theory and local bond averaging approach. She has published 16 journal articles.

Chang Q. Sun, FRSC, FInstP, received his Ph.D. degree in 1996 at Murdoch University, Australia. With research interest in surface, interface, and low-dimensional physics and chemistry, he has been working on the very-low-energy electron diffraction and STM/S analysis of C, N, and O chemisorption bonding dynamics, size dependence of nanostructures, and the thermo-mechanical behavior of low-dimensional systems with development of the bond-order–length–strength correlation, nonbonding electron polarization, the local bond averaging approach, and the zone-resolved photoelectron quantitative spectroscopy. He has published 250 journal articles with over 4000 citations.

ACKNOWLEDGMENTS

Financial support from NSF (Nos. 11002121, and 11172254) of China and the National Key Laboratory of New Ceramics and Process Engineering at Tsinghua University is gratefully acknowledged.

REFERENCES

(1) von Wenckstern, H.; Schmidt, H.; Brandt, M.; Lajn, A.; Pickenhain, R.; Lorenz, M.; Grundmann, M.; Hofmann, D. M.; Polity, A.; Meyer, B. K.; Saal, H.; Binnewies, M.; Börger, A.; Becker, K. D.; Tikhomirov, V. A.; Jug, K. *Prog. Solid State Chem.* **2009**, *37*, 153.
(2) (a) Dai, S.; Dunn, M. L.; Park, H. S. *Nanotechnology* **2010**, *21*, 445707. (b) Dal Corso, A.; Posternak, M.; Resta, R.; Baldereschi, A. *Phys. Rev. B* **1994**, *50*, 10715.
(3) Mi, W. B.; Bai, H. L.; Liu, H.; Sun, C. Q. *J. Appl. Phys.* **2007**, *101*, 023904.
(4) (a) Sun, C. Q. *Nanoscale* **2010**, *2*, 1930. (b) Chattopadhyay, S.; Neogi, S. K.; Sarkar, A.; Mukadam, M. D.; Yusuf, S. M.; Banerjee, A.; Bandyopadhyay, S. *J. Magn. Magn. Mater.* **2011**, *323*, 363. (c) He, F. Q.; Zhao, Y. P. *Appl. Phys. Lett.* **2006**, *88*, 193113.
(5) Xu, S.; Wang, Z. L. *Nano Res.* **2011**, *4*, 1013.
(6) (a) Zang, J. F.; Li, C. M.; Cui, X. Q.; Wang, J. X.; Sun, X. W.; Dong, H.; Sun, C. Q. *Electroanalysis* **2007**, *19*, 1008. (b) Zhao, Z. W.; Lei, W.; Zhang, X. B.; Wang, B. P.; Jiang, H. L. *Sensors* **2010**, *10*, 1216. (c) Pearton, S. J.; Ren, F.; Wang, Y. L.; Chu, B. H.; Chen, K. H.; Chang, C. Y.; Lim, W.; Lin, J. S.; Norton, D. P. *Prog. Mater. Sci.* **2010**, *55*, 1. (d) Huang, J.; Wan, Q. *Sensors* **2009**, *9*, 9903.
(7) Wang, Z. L. *Nano Today* **2010**, *5*, 540.
(8) (a) Gershon, T. *Mater. Sci. Technol.* **2011**, *27*, 1357. (b) Xu, F.; Sun, L. T. *Energy Environ. Sci.* **2011**, *4*, 818.
(9) (a) Liu, X. J.; Pan, L. K.; Lv, T.; Lu, T.; Zhu, G.; Sun, Z.; Sun, C. Q. *Catal. Sci. Technol.* **2011**, *1*, 1189. (b) Zhu, G. A.; Lv, T. A.; Pan, L. K.; Sun, Z.; Sun, C. Q. *J. Alloys Compd.* **2011**, *509*, 362. (c) Liu, X. J.; Pan, L. K.; Sun, Z.; Chen, Y. M.; Yang, X. X.; Yang, L. W.; Zhou, Z. F.; Sun, C. Q. *J. Appl. Phys.* **2011**, *110*, 044322. (d) Wang, M.; Fei, G. T.; Zhang, L. D. *Nanoscale Res. Lett.* **2010**, *5*, 1800.

(10) (a) Agrawal, R.; Espinosa, H. D. *Nano Lett.* **2011**, *11*, 786. (b) Wei, Y. G.; Wu, W. Z.; Guo, R.; Yuan, D. J.; Das, S. M.; Wang, Z. L. *Nano Lett.* **2010**, *10*, 3414. (c) Lin, C. Y.; Lai, Y. H.; Chen, H. W.; Chen, J. G.; Kung, C. W.; Vittal, R.; Ho, K. C. *Energy Environ. Sci.* **2011**, *4*, 3448.
(11) (a) Fu, M.; Zhou, J.; Yu, J. H. *J. Phys. Chem. C* **2010**, *114*, 9216. (b) Fu, M.; Zhou, J. *J. Electrochem. Soc.* **2010**, *157*, D450.
(12) Zhang, Y. P.; Sun, X. W.; Pan, L. K.; Li, H. B.; Sun, Z.; Sun, C. Q.; Tay, B. K. *J. Alloys Compd.* **2009**, *480*, L17.
(13) Vanmaekelbergh, D.; van Vugt, L. K. *Nanoscale* **2011**, *3*, 2783.
(14) Zhai, T. Y.; Li, L.; Ma, Y.; Liao, M. Y.; Wang, X.; Fang, X. S.; Yao, J. N.; Bando, Y.; Golberg, D. *Chem. Soc. Rev.* **2011**, *40*, 2986.
(15) Rasmussen, J. W.; Martinez, E.; Louka, P.; Wingettt, D. G. *Expert Opin. Drug Delivery* **2010**, *7*, 1063.
(16) (a) Zhang, Y. M.; Lan, D.; Wang, Y. R.; Cao, H.; Zhao, Y. P. *J. Colloid Interface Sci.* **2010**, *351*, 288. (b) Wang, B. B.; Zhao, Y. P.; Yu, T. X. *J. Adhes. Sci. Technol.* **2011**, *25*, 93. (c) Wang, B. B.; Feng, J. T.; Zhao, Y. P.; Yu, T. X. *J. Adhes. Sci. Technol.* **2010**, *24*, 2693.
(17) (a) Shi, L. X.; Li, X. Y. *J. Lumin.* **2011**, *131*, 834. (b) Choi, Y. S.; Kang, J. W.; Hwang, D. K.; Park, S. J. *IEEE Trans. Electron Devices* **2010**, *57*, 26.
(18) (a) Herng, T. S.; Lau, S. P.; Wang, L.; Zhao, B. C.; Yu, S. F.; Tanemura, M.; Akaike, A.; Teng, K. S. *Appl. Phys. Lett.* **2009**, *95*, 012505. (b) Herng, T. S.; Lau, S. P.; Wei, C. S.; Wang, L.; Zhao, B. C.; Tanemura, M.; Akaike, Y. *Appl. Phys. Lett.* **2009**, *95*, 133103.
(19) (a) Wu, J. S.; Xue, D. F. *Sci. Adv. Mater.* **2011**, *3*, 127. (b) Klingshirn, C.; Fallert, J.; Zhou, H.; Sartor, J.; Thiele, C.; Maier-Flaig, F.; Schneider, D.; Kalt, H. *Phys. Status Solidi B: Basic Solid State Phys.* **2010**, *247*, 1424. (c) Wang, Z. L. *Mater. Sci. Eng. R: Rep.* **2009**, *64*, 33. (d) Klingshirn, C. *ChemPhysChem: Eur. J. Chem. Phys. Phys. Chem.* **2007**, *8*, 782.
(20) (a) Yan, C. L.; Xue, D. F. *Adv. Mater.* **2008**, *20*, 1055. (b) Gao, P. X.; Ding, Y.; Mai, W. J.; Hughes, W. L.; Lao, C. S.; Wang, Z. L. *Science* **2005**, *309*, 1700.
(21) (a) Frenken, J. W. M.; Veen, J. F. v. d. *Phys. Rev. Lett.* **1985**, *54*, 134. (b) Sun, C. Q. *Prog. Solid State Chem.* **2007**, *35*, 1.
(22) Dutta, S.; Chattopadhyay, S.; Sarkar, A.; Chakrabarti, M.; Sanyal, D.; Jana, D. *Prog. Mater. Sci.* **2009**, *54*, 89.
(23) (a) Chen, C. Q.; Shi, Y.; Zhang, Y. S.; Zhu, J.; Yan, Y. J. *Phys. Rev. Lett.* **2006**, *96*, 075505. (b) Hoffmann, S.; Östlund, F.; Michler, J.; Fan, H. J.; Zacharias, M.; Christiansen, S. H.; Ballif, C. *Nanotechnology* **2007**, *18*, 205503. (c) Cao, G. X.; Chen, X. *Phys. Rev. B* **2007**, *76*, 165407. (d) Moon, W.; Hwang, H. *Nanotechnology* **2008**, *19*, 225703. (e) Agrawal, R.; Peng, B.; Gdoutos, E. E.; Espinosa, H. D. *Nano Lett.* **2008**, *8*, 3668. (f) Cao, G. X.; Chen, X. *Int. J. Solids Struct.* **2008**, *45*, 1730.
(24) (a) Lin, K.-F.; Cheng, H.-M.; Hsu, H.-C.; Lin, L.-J.; Hsieh, W.-F. *Chem. Phys. Lett.* **2005**, *409*, 208. (b) Cao, B.; Cai, W.; Zeng, H. *Appl. Phys. Lett.* **2006**, *88*, 161101. (c) Li, J. B.; Wang, L. W. *Phys. Rev. B* **2005**, *72*, 125325. (d) Li, Y. Q.; Yang, Y.; Sun, C. Q.; Fu, S. Y. *J. Chem. Phys. C* **2008**, *112*, 17397. (e) Tay, Y. Y.; Li, S.; Sun, C. Q.; Chen, P. *Appl. Phys. Lett.* **2006**, *88*, 173118.
(25) (a) Guisbiers, G.; Pereira, S. *Nanotechnology* **2007**, *18*, 435710. (b) Su, X.; Zhang, Z. J.; Zhu, M. M. *Appl. Phys. Lett.* **2006**, *88*, 061913. (c) Fang, T.-H.; Chang, W.-J.; Chiu, J.-W. *Microelectron. J.* **2006**, *37*, 722. (d) Zhang, L.; Huang, H. C. *Appl. Phys. Lett.* **2007**, *90*, 023115. (e) Liang, J. Y.; Guo, L.; Xu, H. B.; Jing, L.; Dong, L. X.; Hua, W. Z.; Yu, W. Z.; Weber, J. *J. Cryst. Growth* **2003**, *252*, 226. (f) Mori, Y.; Niiya, N.; Ukegawa, K.; Mizuno, T.; Takarabe, K.; Ruoff, A. L. *Phys. Status Solidi (b)* **2004**, *241*, 3198. (g) Bates, C. H.; White, W. B.; Roy, R. *Science* **1962**, *137*, 993.
(26) (a) Yang, C. C.; Li, S. *J. Phys. Chem. B* **2008**, *112*, 14193. (b) Lin, K.-F.; Cheng, H.-M.; Hsu, H.-C.; Hsieh, W.-F. *Appl. Phys. Lett.* **2006**, *88*, 263117. (c) Yadav, H. K.; Gupta, V.; Sreenivas, K.; Singh, S. P.; Sundarakannan, B.; Katiyar, R. S. *Phys. Rev. Lett.* **2006**, *97*, 085502. (d) Chassaing, P. M.; Demangeot, F.; Combe, N.; Saint-Macary, L.; Kahn, M. L.; Chaudret, B. *Phys. Rev. B* **2009**, *79*, 155314. (e) Combe, N.; Chassaing, P.-M.; Demangeot, F. *Phys. Rev. B* **2009**, *79*, 045408. (f) Chowdhury, R.; Adhikari, S.; Scarpa, F. *Appl. Phys. a: Mater. Sci. Process.* **2011**, *102*, 301.
(27) Zhang, K. M.; Zhao, Y. P.; He, F. Q.; Liu, D. Q. *Chin. J. Chem. Phys.* **2007**, *20*, 721.
(28) Han, X. H.; Wang, G. Z.; Wang, Q. T.; Cao, L.; Liu, R.; Zou, B. S.; Hou, J. G. *Appl. Phys. Lett.* **2005**, *86*, 223106.
(29) Xu, F.; Qin, Q.; Mishra, A.; Gu, Y.; Zhu, Y. *Nano Res.* **2010**, *3*, 271.
(30) Zang, J. F.; Bao, L. H.; Webb, R. A.; Li, X. D. *Nano Lett.* **2011**, *11*, 4885.
(31) (a) Viswanatha, R.; Sapra, S.; Satpati, B.; Satyam, P. V.; Dev, B. N.; Sarma, D. D. *J. Mater. Chem.* **2004**, *14*, 661. (b) Meulenkamp, E. A. *J. Phys. Chem. B* **1998**, *102*, 5566. (c) Cheng, H. M.; Lin, K. F.; Hsu, H. C.; Hsieh, W. F. *Appl. Phys. Lett.* **2006**, *88*, 261909. (d) Guo, L.; Yang, S.; Yang, C.; Yu, P.; Wang, J.; Ge, W.; Wong, G. K. L. *Appl. Phys. Lett.* **2000**, *76*, 2901.
(32) (a) Yi, G.-C.; Wang, C. R.; Park, W. I. *Semicond. Sci. Technol.* **2005**, *20*, S22. (b) Chen, C.-W.; Chen, K.-H.; Shen, C.-H.; Ganguly, A.; Chen, L.-C.; Wu, J.-J.; Wen, H.-I.; Pong, W.-F. *Appl. Phys. Lett.* **2006**, *88*, 241905. (c) Yang, Y. H.; Chen, X. Y.; Feng, Y.; Yang, G. W. *Nano Lett.* **2007**, *7*, 3879. (d) Zheng, C. C.; Xu, S. J.; Ning, J. Q.; Zhang, S. F.; Wang, J. Y.; Che, C. M.; Hao, J. H. *J. Appl. Phys.* **2011**, *109*, 013528.
(33) Wang, X. D.; Ding, Y.; Summers, C. J.; Wang, Z. L. *J. Phys. Chem. B* **2004**, *108*, 8773.
(34) Yuan, Q. Z.; Zhao, Y. P.; Li, L. M.; Wang, T. H. *J. Phys. Chem. C* **2009**, *113*, 6107.
(35) (a) Wu, H.; Cheng, X.; Zhang, H.; Liu, Z. *Philos. Mag. Lett.* **2008**, *88*, 181. (b) Fei, Y.; Cheng, S.; Shi, L. B.; Yuan, H. K. *J. Synth. Cryst.* **2009**, *38*, 1527. (c) Swarnakar, A. K.; Donzel, L.; Vleugels, J.; Van der Biest, O. *J. Eur. Ceram. Soc.* **2009**, *29*, 2991. (d) Ursaki, V. V.; Tiginyanu, I. M.; Zalamai, V. V.; Rusu, E. V.; Emelchenko, G. A.; Masalov, V. M.; Samarov, E. N. *Phys. Rev. B* **2004**, *70*, 155204. (e) Shan, W.; Walukiewicz, W.; Ager, J. W. III; Yu, K. M.; Zhang, Y.; Mao, S. S.; Kling, R.; Kirchner, C.; Waag, A. *Appl. Phys. Lett.* **2005**, *86*, 153117. (f) Tarnow, V. *J. Phys. D: Appl. Phys.* **1969**, *2*, 1383. (g) Chen, S. J.; Liu, Y. C.; Shao, C. L.; Xu, C. S.; Liu, Y. X.; Liu, C. Y.; Zhang, B. P.; Wang, L.; Liu, B. B.; Zou, G. T. *Appl. Phys. Lett.* **2006**, *88*, 133127. (h) Su, F. H.; Wang, W. J.; Ding, K.; Li, G. H.; Liu, Y. F.; Joly, A. G.; Chen, W. *J. Phys. Chem. Solids* **2006**, *67*, 2376. (i) Li, J. W.; Yang, L. W.; Zhou, Z. F.; Chu, P. K.; Wang, X. H.; Zhou, J.; Li, L. T.; Sun, C. Q. *J. Chem. Phys. C* **2010**, *114*, 13370. (j) Sun, J.; Wang, H. T.; He, J. L.; Tian, Y. J. *Phys. Rev. B* **2005**, *71*, 125132.
(36) (a) Li, K. Y.; Wang, X. T.; Zhang, F. F.; Xue, D. F. *Phys. Rev. Lett.* **2008**, *100*, 235504. (b) Li, K. Y.; Ding, Z. S.; Xue, D. F. *Phys. Status Solidi B: Basic Solid State Phys.* **2011**, *248*, 1227.
(37) (a) Gao, F. M.; He, J. L.; Wu, E. D.; Liu, S. M.; Yu, D. L.; Li, D. C.; Zhang, S. Y.; Tian, Y. J. *Phys. Rev. Lett.* **2003**, *91*, 015502. (b) He, J. L.; Wu, E. D.; Wang, H. T.; Liu, R. P.; Tian, Y. J. *Phys. Rev. Lett.* **2005**, *94*, 015504.
(38) (a) Qi, J. S.; Shi, D. N.; Jia, J. M. *Nanotechnology* **2008**, *19*, 435707. (b) Asthana, A.; et al. *Nanotechnology* **2011**, *22*, 265712. (c) Zhang, L.; Huang, H. *Appl. Phys. Lett.* **2006**, *89*, 183111.
(39) Liang, H.; Upmanyu, M.; Huang, H. *Phys. Rev. B* **2005**, *71*, 241403.
(40) Chan, W. K.; Zhang, T. Y. *J. Appl. Phys.* **2010**, 107.
(41) (a) Dai, D. C.; Xu, S. J.; Shi, S. L.; Xie, M. H. *Opt. Lett.* **2005**, *30*, 3377. (b) Shi, S. L.; Li, G. Q.; Xu, S. J.; Zhao, Y.; Chen, G. H. *J. Phys. Chem. B* **2006**, *110*, 10475. (c) Ye, J.; Zhao, Y.; Tang, L.; Chen, L.-M.; Luk, C. M.; Yu, S. F.; Lee, S. T.; Lau, S. P. *Appl. Phys. Lett.* **2011**, *98*, 263101. (d) Pan, L. K.; Liu, X. J.; Sun, Z.; Sun, C. Q. *Prog. Mater. Sci.*, in press.
(42) Pesika, N. S.; Hu, Z.; Stebe, K. J.; Searson, P. C. *J. Phys. Chem. B* **2002**, *106*, 6985.
(43) Qin, G. G.; Song, H. Z.; Zhang, B. R.; Lin, J.; Duan, J. Q.; Yao, G. Q. *Phys. Rev. B* **1996**, *54*, 2548.
(44) Pan, L. K.; Sun, C. Q. *J. Appl. Phys.* **2004**, *95*, 3819.
(45) (a) Cheng, H.-M.; Lin, K.-F.; Hsu, C. H.; Lin, C.-J.; Lin, L.-J.; Hsieh, W.-F. *J. Phys. Chem. B* **2005**, *109*, 18385. (b) Calizo, I.;

Alim, K. A.; Fonoberov, V. A.; Krishnakumar, S.; Shamsa, M.; Balandin, A. A.; Kurtz, R. *Proc. SPIE* **2007**, *6481*, 64810N.
(46) (a) Cheng, W.; Ren, S.-F. *Phys. Rev. B* **2002**, *65*, 205305. (b) Zi, J. *Appl. Phys. Lett.* **1996**, *69*, 200. (c) Viera, G. *J. Appl. Phys.* **2001**, *90*, 4175.
(47) Schaefer, C.; Laugwitz, M. *Ann. Phys.* **1907**, *23*, 599.
(48) Liang, L.-H.; Shen, C.-M.; Chen, X.-P.; Liu, W.-M.; Gao, H.-J. *J. Phys.: Condens. Matter* **2004**, *16*, 267.
(49) Diéguez, A. *J. Appl. Phys.* **2001**, *90*, 1550.
(50) (a) Anastassakis, E.; Liarokapis, E. *J. Appl. Phys.* **1987**, *62*, 3346. (b) Iqbal, Z.; Veprek, S. *J. Phys. C: Solid State Phys.* **1982**, *15*, 377.
(51) (a) Richter, H.; Wang, Z. P.; Ley, L. *Solid State Commun.* **1981**, *39*, 625. (b) Campbell, I. H.; Fauchet, P. M. *Solid State Commun.* **1986**, *58*, 739.
(52) Sun, C. Q. *Prog. Mater. Sci.* **2003**, *48*, 521.
(53) Janotti, A.; Van de Walle, C. G. *Rep. Prog. Phys.* **2009**, *72*, 126501.
(54) (a) Mirjalili, M.; Vahdati-Khaki, J. *J. Phys. Chem. Solids* **2008**, *69*, 2116. (b) Hu, M.; Poulikakos, D.; Grigoropoulos, C. P.; Pan, H. *J. Chem. Phys.* **2010**, *132*, 164504. (c) Wang, J.; Kulkarni, A. J.; Ke, F. J.; Bai, Y. L.; Zhou, M. *Comput. Methods Appl. Mech. Eng.* **2008**, *197*, 3182.
(55) (a) Jiang, A.; Awasthi, N.; Kolmogorov, A. N.; Setyawan, W.; ouml; rjesson, A.; Bolton, K.; Harutyunyan, A. R.; Curtarolo, S. *Phys. Rev. B* **2007**, *75*, 205426. (b) Silvestri, M. R.; Schroeder, J. *J. Phys.: Condens. Matter* **1995**, *7*, 8519. (c) Ricolleau, C.; Audinet, L.; Gandais, M.; Gacoin, T. *Eur. Phys. J. D: At., Mol., Opt. Plasma Phys.* **1999**, *9*, 565.
(56) Wu, J. S.; Xue, D. F. *CrystEngComm* **2011**, *13*, 1966.
(57) Sun, C. Q.; Wang, Y.; Tay, B. K.; Li, S.; Huang, H.; Zhang, Y. B. *J. Phys. Chem. B* **2002**, *106*, 10701.
(58) Couchman, P. R.; Jesser, W. A. *Nature* **1977**, *269*, 481.
(59) Qi, W. H.; Wang, M. P. *Mater. Chem. Phys.* **2004**, *88*, 280.
(60) (a) Wang, J.; Duan, H. L.; Huang, Z. P.; Karihaloo, B. L. *Proc. R. Soc. A: Math., Phys. Eng. Sci.* **2006**, *462*, 1355. (b) Jiang, Q.; Zhang, Z.; Li, J. C. *Acta Mater.* **2000**, *48*, 1469.
(61) Wachtman, J. B.; Tefft, W. E.; Lam, D. G.; Apstein, C. S. *Phys. Rev.* **1961**, *122*, 1754.
(62) (a) Alers, G. A.; Waldorf, D. L. *Phys. Rev. Lett.* **1961**, *6*, 677. (b) Chang, R.; Graham, L. J. *J. Appl. Phys.* **1966**, *37*, 3778.
(63) Anderson, O. L. *Phys. Rev.* **1966**, *144*, 553.
(64) Garai, J.; Laugier, A. *J. Appl. Phys.* **2007**, *101*, 023514.
(65) (a) Mead, D. G.; Wilkinson, G. R. *J. Raman Spectrosc.* **1977**, *6*, 123. (b) Cusco, R.; Alarcon-Llado, E.; Ibanez, J.; Artus, L.; Jimenez, J.; Wang, B.; Callahan, M. J. *Phys. Rev. B (Condens. Matter Mater. Phys.)* **2007**, *75*, 165202. (c) Aku-Leh, C.; Zhao, J.; Merlin, R.; Menendez, J.; Cardona, M. *Phys. Rev. B* **2005**, *71*, 205211. (d) Samanta, K.; Bhattacharya, P.; Katiyar, R. S. *Phys. Rev. B (Condens. Matter Mater. Phys.)* **2007**, *75*, 035208. (e) Serrano, J.; Romero, A. H.; Manjon, F. J.; Lauck, R.; Cardona, M.; Rubio, A. *Phys. Rev. B* **2004**, *69*, 094306. (f) Decremps, F.; Pellicer-Porres, J.; Saitta, A. M.; Chervin, J.-C.; Polian, A. *Phys. Rev. B* **2002**, *65*, 092101. (g) Panchal, V.; Ghosh, S.; Gohil, S.; Kulkarni, N.; Ayyub, P. *J. Phys.: Condens. Matter* **2008**, *20*, 345224. (h) Mitra, S. S.; Brafman, O.; Daniels, W. B.; Crawford, R. K. *Phys. Rev.* **1969**, *186*, 942. (i) Reparaz, J. S. *Appl. Phys. Lett.* **2010**, *96*, 231906.
(66) Domènech-Amador, N.; Cuscó, R.; Artús, L.; Yamaguchi, T.; Nanishi, Y. *Phys. Rev. B* **2011**, *83*, 245203.
(67) Alim, K. A. *J. Appl. Phys.* **2005**, *97*, 124313.
(68) Tang, H.; Herman, I. P. *Phys. Rev. B* **1991**, *43*, 2299.
(69) (a) Eom, S. H.; Yu, Y. M.; Choi, Y. D.; Kim, C. S. *J. Cryst. Growth* **2005**, *284*, 166. (b) Alawadhi, H.; Tsoi, S.; Lu, X.; Ramdas, A. K.; Grimsditch, M.; Cardona, M.; Lauck, R. *Phys. Rev. B* **2007**, *75*, 205207.
(70) Varshni, Y. P. *Physica* **1967**, *34*, 149.
(71) Liu, J.; Vohra, Y. K. *Phys. Rev. Lett.* **1994**, *72*, 4105.
(72) Liu, C.; Yun, F.; Morkoc, H. *J. Mater. Sci.-Mater. Electron.* **2005**, *16*, 555.
(73) Gao, X. D.; Jiang, E. Y.; Liu, H. H.; Mi, W. B.; Li, Z. Q.; Wu, P.; Bai, H. L. *Appl. Surf. Sci.* **2007**, *253*, 5431.
(74) (a) Matsumoto, Y.; Murakami, M.; Shono, T.; Hasegawa, T.; Fukumura, T.; Kawasaki, M.; Ahmet, P.; Chikyow, T.; Koshihara, S.; Koinuma, H. *Science* **2001**, *291*, 854. (b) Mi, W. B.; Jiang, E. Y.; Bai, H. L. *J. Magn. Magn. Mater.* **2009**, *321*, 2472.
(75) Venkatesan, M.; Stamenov, P.; Dorneles, L. S.; Gunning, R. D.; Bernoux, B.; Coey, J. M. D. *Appl. Phys. Lett.* **2007**, *90*, 242508.
(76) Ramachandran, S.; Tiwari, A.; Narayan, J.; Prater, J. T. *Appl. Phys. Lett.* **2005**, *87*, 172502.
(77) (a) Kumar, D.; Antifakos, J.; Blamire, M. G.; Barber, Z. H. *Appl. Phys. Lett.* **2004**, *84*, 5004. (b) Singh, R. K.; Wu, S. Y.; Liu, H. X.; Gu, L.; Smith, D. J.; Newman, N. *Appl. Phys. Lett.* **2005**, *86*, 012504.
(78) (a) Yang, J. H.; Cheng, Y.; Liu, Y.; Ding, X.; Wang, Y. X.; Zhang, Y. J.; Liu, H. L. *Solid State Commun.* **2009**, *149*, 1164. (b) Lee, H. J.; Jeong, S. Y.; Cho, C. R.; Park, C. H. *Appl. Phys. Lett.* **2002**, *81*, 4020.
(79) (a) Coey, J. M. D. *Curr. Opin. Solid State Mater. Sci.* **2006**, *10*, 83. (b) Hou, D. L.; Zhao, R. B.; Wei, Y. Y.; Zhen, C. M.; Pan, C. F.; Tang, G. D. *Curr. Appl. Phys.* **2010**, *10*, 124.
(80) (a) Tian, D. L.; Zhang, X. F.; Zhai, J.; Jiang, L. *Langmuir* **2011**, *27*, 4265. (b) Wu, X. D.; Zheng, L. J.; Wu, D. *Langmuir* **2005**, *21*, 2665. (c) Liu, H.; Feng, L.; Zhai, J.; Jiang, L.; Zhu, D. B. *Langmuir* **2004**, *20*, 5659. (d) Zhang, J. L.; Huang, W. H.; Han, Y. C. *Langmuir* **2006**, *22*, 2946.
(81) (a) Yu, J. G.; Yu, X. X. *Environ. Sci. Technol.* **2008**, *42*, 4902. (b) Karunakaran, C.; Senthilvelan, S.; Karuthapandian, S. *Sol. Energy Mater. Sol. Cells* **2005**, *89*, 391. (c) Neelavannan, M. G.; Basha, C. A. *Environ. Technol.* **2011**, *32*, 825.
(82) (a) Pan, F.; Song, C.; Liu, X. J.; Yang, Y. C.; Zeng, F. *Mater. Sci. Eng. R: Rep.* **2008**, *62*, 1. (b) Coey, J. M. D.; Venkatesan, M.; Fitzgerald, C. B. *Nat. Mater.* **2005**, *4*, 173.
(83) Céspedes, E.; Laguna-Marco, M. A.; Jiménez-Villacorta, F.; Chaboy, J.; Boada, R.; Guglieri, C.; Andrés, A. d.; Prieto, C. *J. Phys. Chem. C* **2011**, DOI: 10.1021/jp208929w.
(84) Hong, N. H.; Sakai, J.; Huong, N. T.; Poirot, N.; Ruyter, A. *Phys. Rev. B* **2005**, *72*, 045336.
(85) (a) Xu, W. G.; Shi, X. F.; Lu, S. X. *Mater. Chem. Phys.* **2011**, *129*, 1042. (b) Adam, N. K. *Nature* **1957**, *180*, 809.
(86) (a) Sun, C. Q.; Sun, Y.; Ni, Y. G.; Zhang, X.; Pan, J. S.; Wang, X. H.; Zhou, J.; Li, L. T.; Zheng, W. T.; Yu, S. S.; Pan, L. K.; Sun, Z. *J. Chem. Phys. C* **2009**, *113*, 20009. (b) Li, J. J.; Zhang, C. H.; Luo, J. B. *Langmuir* **2011**, *27*, 9413. (c) Lee, C.; Choi, C. H.; Kim, C. J. *Phys. Rev. Lett.* **2008**, *101*, 064501.
(87) Roduner, E. *Chem. Soc. Rev.* **2006**, *35*, 583.
(88) Pauling, L. *J. Am. Chem. Soc.* **1935**, *57*, 2680.
(89) Goldschmidt, V. M. *Ber. Dtsch. Chem. Ges.* **1927**, *60*, 1263.
(90) Pauling, L. *J. Phys. Chem.* **1947**, *69*, 542.
(91) Abrahams, E.; Anderson, P. W.; Licciardello, D. C.; Ramakrishnan, T. V. *Phys. Rev. Lett.* **1979**, *42*, 673.
(92) Zheng, W. T.; Sun, C. Q. *Prog. Solid State Chem.* **2006**, *34*, 1.
(93) Zheng, W. T.; Sun, C. Q. *Energy Environ. Sci.* **2011**, *4*, 627.
(94) Sun, C. Q. *Prog. Mater Sci.* **2009**, *54*, 179.
(95) Yang, X. X.; Li, J. W.; Zhou, Z. F.; Wang, Y.; Yang, L. W.; Zheng, W. T.; Sun, C. Q. *Nanoscale* **2011**, DOI: 10.1039/C1NR11280E.
(96) Li, J.; Li, Y. X.; Yu, X.; Ye, W. J.; Sun, C. Q. *J. Phys. D: Appl. Phys.* **2009**, *42*, 045406.
(97) (a) Yan, X. X.; Xu, D. L.; Xue, D. F. *Acta Mater.* **2007**, *55*, 5747. (b) Xu, D. L.; Xue, D. F. *J. Cryst. Growth* **2006**, *286*, 108.
(98) Shpyrko, O. G.; Grigoriev, A. Y.; Steimer, C.; Pershan, P. S.; Lin, B.; Meron, M.; Graber, T.; Gerbhardt, J.; Ocko, B.; Deutsch, M. *Phys. Rev. B* **2004**, *70*, 224206.
(99) Huang, W. J.; Sun, R.; Tao, J.; Menard, L. D.; Nuzzo, R. G.; Zuo, J. M. *Nat. Mater.* **2008**, *7*, 308.
(100) Feibelman, P. J. *Phys. Rev. B* **1996**, *53*, 13740.
(101) Liu, X. J.; Li, J. W.; Zhou, Z. F.; Yang, L. W.; Ma, Z. S.; Xie, G. F.; Pan, Y.; Sun, C. Q. *Appl. Phys. Lett.* **2009**, *94*, 131902.
(102) Ma, S.; Liang, H.; Wang, X.; Zhou, J.; Li, L.; Sun, C. Q. *J. Phys. Chem. C* **2011**, *115*, 20487.

(103) (a) Decremps, F.; Datchi, F.; Saitta, A. M.; Polian, A.; Pascarelli, S.; Di Cicco, A.; Iti, J. P.; Baudelet, F. *Phys. Rev. B* **2003**, *68*, 015502. (b) Sowa, H.; Ahsbahs, H. *J. Appl. Crystallogr.* **2006**, *39*, 169.
(104) Karzel, H.; Potzel, W.; Köfferlein, M.; Schiessl, W.; Steiner, M.; Hiller, U.; Kalvius, G. M.; Mitchell, D. W.; Das, T. P.; Blaha, P.; Schwarz, K.; Pasternak, M. P. *Phys. Rev. B* **1996**, *53*, 11425.
(105) Chen, Z. W.; Sun, C. Q.; Zhou, Y. C.; Gang, O. Y. *J. Chem. Phys. C* **2008**, *112*, 2423.
(106) Desgreniers, S. *Phys. Rev. B* **1998**, *58*, 14102.
(107) Pan, L. K.; Gu, M. X.; Ouyang, G.; Sun, C. Q. *Key Eng. Mater.* **2010**, *444*, 17.
(108) Armstrong, J. N.; Hua, S. Z.; Chopra, H. D. *Phys. Status Solidi (RRL)* **2011**, DOI: 10.1002/pssr.201105541.
(109) Li, K. Y.; Ding, Z. S.; Xue, D. F. *Funct. Mater. Lett.* **2010**, *3*, 241.
(110) Schrouer, P.; Kruger, P.; Pollmann, J. *Phys. Rev. B* **1994**, *49*, 17092.
(111) (a) Oh, D. C.; Kato, T.; Goto, H.; Park, S. H.; Hanada, T.; Yao, T.; Kim, J. J. *Appl. Phys. Lett.* **2008**, *93*, 241907. (b) Chen, Y.; Tuan, N. T.; Segawa, Y.; Ko, H.-j.; Hong, S.-k.; Yao, T. *Appl. Phys. Lett.* **2001**, *78*, 1469.
(112) Ma, D. D. D.; Lee, C. S.; Au, F. C. K.; Tong, S. Y.; Lee, S. T. *Science* **2003**, *299*, 1874.
(113) Li, J. W.; Liu, X. J.; Yang, L. W.; Zhou, Z. F.; Xie, G. F.; Pan, Y.; Wang, X. H.; Zhou, J.; Li, L. T.; Pan, L. K.; Sun, Z.; Sun, C. Q. *Appl. Phys. Lett.* **2009**, *95*, 031906.
(114) Cao, H. L.; Qian, X. F.; Gong, Q.; Du, W. M.; Ma, X. D.; Zhu, Z. K. *Nanotechnology* **2006**, *17*, 3632.
(115) (a) Wang, Y.; Yang, X. X.; Li, J. W.; Zhou, Z. F.; Zheng, W. T.; Sun, C. Q. *Appl. Phys. Lett.* **2011**, *99*, 163109. (b) Yang, X. X.; Li, J. W.; Zhou, Z. F.; Wang, Y.; Zheng, W. T.; Sun, C. Q. *Appl. Phys. Lett.* **2011**, *99*, 133108.
(116) (a) Lindemann, F. A. *Phys. Zeit.* **1910**, *11*, 609. (b) Shi, F. G. *J. Mater. Res.* **1994**, *9*, 1307. (c) Jiang, Q.; Shi, H. X.; Zhao, M. *J. Chem. Phys.* **1999**, *111*, 2176.
(117) Sun, C. Q. *Science in China, G, special issue on Physical Mechanics*, in press.
(118) Khan, A. A. *Acta Crystallogr., Sect. A* **1968**, *24*, 403.
(119) Slack, G. A.; Bartram, S. F. *J. Appl. Phys.* **1975**, *46*, 89.
(120) Hauschild, R.; Priller, H.; Decker, M.; Bruckner, J.; Kalt, H.; Klingshirn, C. *Phys. Status Solidi C* **2006**, *3*, 976.
(121) Gu, M. X.; Pan, L. K.; Tay, B. K.; Sun, C. Q. *J. Raman Spectrosc.* **2007**, *38*, 780.
(122) Vanithakumari, S. C.; Nanda, K. K. *Phys. Lett. A* **2008**, *372*, 6930.
(123) Sun, C. Q.; Shi, Y.; Li, C. M.; Li, S.; Yeung, T. C. A. *Phys. Rev. B* **2006**, *73*, 075408.
(124) Romero-Gómez, P.; Toudert, J.; Sánchez-Valencia, J. R.; Borrás, A.; Barranco, A.; Gonzalez-Elipe, A. R. *J. Phys. Chem. C* **2010**, *114*, 20932.
(125) Dutta, S.; Chattopadhyay, S.; Jana, D.; Banerjee, A.; Manik, S.; Pradhan, S. K.; Sutradhar, M.; Sarkar, A. *J. Appl. Phys.* **2006**, *100*, 114328.
(126) Singh, V. N.; Mehta, B. R. *J. Nanosci. Nanotechnol.* **2005**, *5*, 431.
(127) Kang, H. S.; Kang, J. S.; Kim, J. W.; Lee, S. Y. *J. Appl. Phys.* **2004**, *95*, 1246.
(128) Li, J. W.; Yang, L. W.; Zhou, Z. F.; Liu, X. J.; Xie, G. F.; Pan, Y.; Sun, C. Q. *J. Phys. Chem. B* **2010**, *114*, 1648.
(129) Huso, J.; Morrison, J. L.; Hoeck, H.; Chen, X.-B.; Bergman, L.; Jokela, S. J.; McCluskey, M. D.; Zheleva, T. *Appl. Phys. Lett.* **2006**, *89*, 171909.
(130) Ouyang, G.; Sun, C. Q.; Zhu, W. G. *J. Phys. Chem. B* **2008**, *112*, 5027.
(131) Grzanka, E.; Gierlotka, S.; Stelmakh, S.; Palosz, B.; Strachowski, T.; Swiderska-Sroda, A.; Kalisz1, G.; Lojkowski, W.; Porsch, F. *Zeit. Kristallogr. Suppl.* **2006**, *23*, 337.
(132) Jiang, J. Z.; Olsen, J. S.; Gerward, L.; Frost, D.; Rubie, D.; Peyronneau, J. *Europhys. Lett.* **2000**, *50*, 48.
(133) Sun, C. Q.; Nie, Y.; Pan, J. S.; Zhang, X.; Ma, S. Z.; Wang, Y.; Zheng, W. T. *RSC Adv.*, DOI:10.1039/C2RA00512C.
(134) Volnianska, O.; Boguslawski, P. *J. Phys.: Condens. Matter* **2010**, *22*, 073202.
(135) Sun, C. Q.; Wang, Y.; Nie, Y. G.; Mehta, B. R.; Khanuja, M.; Shivaprasad, S. M.; Sun, Y.; Pan, J. S.; Pan, L. K.; Sun, Z. *Phys. Chem. Chem. Phys.* **2010**, *12*, 3131.
(136) Sun, C. Q.; Wang, Y.; Nie, Y. G.; Sun, Y.; Pan, J. S.; Pan, L. K.; Sun, Z. *J. Chem. Phys. C* **2009**, *113*, 21889.
(137) Nie, Y. G.; Zhang, X.; Ma, S. Z.; Wang, Y.; Pan, J. S.; Sun, C. Q. *Phys. Chem. Chem. Phys.* **2011**, *13*, 12640.
(138) Sun, C. Q. *Phys. Rev. B* **2004**, *69*, 045105.
(139) (a) Tay, Y. Y.; Tan, T. T.; Liang, M. H.; Boey, F.; Li, S. *Phys. Chem. Chem. Phys.* **2010**, *12*, 6008. (b) Tay, Y. Y.; Tan, T. T.; Boey, F.; Liang, M. H.; Ye, J.; Zhao, Y.; Norby, T.; Li, S. *Phys. Chem. Chem. Phys.* **2010**, *12*, 2373.
(140) Liu, X.; Bauer, M.; Bertagnolli, H.; Roduner, E.; van Slageren, J.; Phillipp, F. *Phys. Rev. Lett.* **2006**, *97*, 253401.
(141) Yamamoto, Y.; Miura, T.; Nakae, Y.; Teranishi, T.; Miyake, M.; Hori, H. *Phys. B: Condens. Matter* **2003**, *329*, 1183.